Renewable Energy 159 (2020) 954–972

Contents lists available at ScienceDirect

Renewable Energy

journal homepage: www.elsevier.com/locate/renene

Solar energy harvesting on-board small satellites

Fiona Leverone [a, b, *], Matteo Pini [a], Angelo Cervone [b], Eberhard Gill [b]

[a] Department of Propulsion and Power, Delft University of Technology, Kluyverweg 1, 2629, HS, Delft, the Netherlands
[b] Department of Space Systems Engineering, Delft University of Technology, Kluyverweg 1, 2629, HS, Delft, the Netherlands

ARTICLE INFO

Article history:
Received 30 January 2020
Received in revised form
25 May 2020
Accepted 31 May 2020
Available online 8 June 2020

Keywords:
Micro-ORC turbines
Radial-inflow turbine
Solar concentration
Phase change material
Optimisation

ABSTRACT

Small satellites are receiving increased recognition in the space domain due to their reduced associated launch costs and shorter lead time when compared to larger satellites. However, this advantage is often at the expense of mission capabilities, such as available electrical power and propulsion. A possible solution is to shift from the conventional solar photovoltaic and battery configuration to a micro-Organic Rankine Cycle (ORC) and thermal energy storage system that uses the waste energy from a solar thermal propulsion system. However, limited literature is available on micro-ORC systems, which are capable of producing a few hundred Watts of electrical power. This paper describes the proposed system layout and model of the integrated micro-ORC system, for various working fluids such as Toluene, Hexamethyldisiloxane (MM), and Octamethylcyclotetrasiloxane (D4). Toluene has been identified as a promising working fluid candidate resulting in a power generation system volume fraction of 18% for a 215 kg Low Earth Orbit satellite. The micro-ORC system is capable of producing 200 W of electrical power. The design provides high specific energies of at least 500 Wh/kg but, has a low shared specific power of 10 W/kg. A preliminary design of the micro-turbine provides a conservative total-to-static efficiency of 57%.

1. Introduction

The increase of electrical power consumption required by small satellites boosted the need for on-board power sources that have high energy and power densities. This increase is especially important for future planned interplanetary missions proposed by NASA. Future missions are estimated to need power densities in the range of 150 and 250W/kg [1] and specific energies greater than 250 Wh/kg [2]. Conventionally, small satellite power systems consist of photovoltaic technologies which have a specific power from around 20W/kg to 100W/kg [3,4]. Power systems can also include an on-board energy storage device, with advanced lithium-polymer or -ion batteries being the most commonly used. These batteries have specific energies between 150 and 250 Wh/kg [5]. These systems may not be suitable for future missions. Therefore, alternative power systems should be investigated. A possible alternative system that has the potential to offer high power densities is the micro-organic Rankine Cycle (ORC) system [6]. Here micro refers to power levels in the range of 100–500W.

Power systems are not the only crucial sub-system for satellites. To further extend the capabilities of small satellites for future missions, a propulsion system is also required. Solar thermal propulsion (STP) has been identified as a possible cost-effective solution [7]. STP is a system that generates thrust by using concentrated solar radiation to heat a propellant to temperatures of more than 1500K, such to increase the performance over conventional propulsion systems. Coupling an STP system with a micro-ORC system, as shown in Fig. 1, could improve the system efficiency to develop small high-performance satellites by harvesting the energy from the STP receiver to co-generate electrical power and propulsion [6]. The waste heat could also be used for on-board thermal control. The major challenge with integrating an ORC with an STP system for space applications is the different operating temperatures. The STP requires propellant temperatures above 1500K to achieve high performance. In contrast, the ORC has a maximum operating temperature of approximately 600K, depending on the working fluid and its corresponding thermal stability limit. Available literature reports the thermal stability limit for MM to be 300°C [8] and as high as 400°C for cyclic siloxanes [9,10] and Toluene [11]. Therefore, this work also investigates the feasibility of using a high-temperature receiver as a hot source for a micro-ORC system.

The idea of using an ORC for power generation in space dates back to the 1960s [12,13]. ORC systems with power capacities on the

* Corresponding author. Department of Propulsion and Power, Delft University of Technology, Kluyverweg 1, 2629, HS, Delft, the Netherlands.
E-mail addresses: F.K.Leverone@tudelft.nl (F. Leverone), M.Pini@tudelft.nl (M. Pini), A.Cervone@tudelft.nl (A. Cervone), E.K.A.Gill@tudelft.nl (E. Gill).

https://doi.org/10.1016/j.renene.2020.05.176

Nomenclature

A	Area
a	Coefficient
b	Blade height
b	Coefficient
b_f	Shadow factor
BPF	Bundle packaging factor
C	Constant
c	Coefficient
$c'_{f,c}$	Modified friction coefficient
$c_{f,c}$	Friction coefficient
D	Diameter
d	Coefficient
F	Objective function
f	Fanning friction factor, Regenerator fin frequency
h	Enthalpy, Heat transfer coefficient, Height
$K(\infty)$	Fully developed Hagenbach factor
K	Wall roughness
L	Latent heat of the PCM, Length
$\overline{L}$	Fibre mass per length
M	Mass, Mach number
MAE	Mean absolute error
N	Number of
Nu	Nusselt number
P	Penalty parameter
p	Pressure
Pr	Prandtl number
$\dot{Q}$	Thermal power
r	Radius
r_c	Radius of curvature
Re	Reynolds number
S	Solar flux
T	Temperature
t	Time, thickness
tc	Tip clearance
u	Circumferential velocity, fluid velocity
V	Volume
v	Absolute velocity
V_{sys}	Total volume of micro-ORC system
W	Eulerian work
w	Relative velocity
$\dot{W}_{net}$	Electrical power output
x	Optimisation input design variable
x^*	Dimensionless axial coordinate for the thermal entrance region
x^+	Dimensionless axial coordinate for the hydrodynamic entrance region
Z	Number of blades

Greek Symbols

α	Absolute flow angle
β	Rectangular duct aspect ratio, Relative flow angle
η	Efficiency
μ	Design objective
Ω	Penalty term
φ	Axial flow coefficient
ρ	Density
θ	percentage predicted within ±30%, Sun half-angle, Loss coefficient
ς	percentage predicted within ± 50%

Subscripts

0	Stator inlet position
1	Stator outlet position
2	Rotor inlet position
3	Rotor outlet position
app	Apparent
b	Optical fibre bundle
cr	Critical
dis	Discharge
ee	Exit
f	Fluid, Optical fibre
fin	Regenerator fins
fric	Skin friction
g	Generator
hb	Hub
inc	Incidence
ins	Insulation
is	Isentropic
loss	Losses
m	Mean, Meridional direction
N	Stator
o	Out
op	Optical system
pcm	Phase change material
pp	Pinch point
R	Rotor
rec	Receiver
sat	Saturated
sc	Spacecraft
sf	Secondary flow
sh	Shroud
tc	Tip clearance
TS	Total-to-static
TT	Total-to-total
u	Circumferential direction
v	Vapour
vf	Film vapour
wf	Working fluid

order of 1–30 kW, were proposed to power the International Space Station. These systems are attractive for space applications as they can have a higher resistance to degradation in the space environment compared to photovoltaic systems [12,13]. In general, Rankine cycles can have better thermal efficiencies than Brayton and Stirling cycles for space applications at a cost of larger radiators [14]. At micro-scales, Rankine cycles can also have better thermal efficiency and higher power density versus Brayton cycles [15]. Rankine cycles can therefore lead to lighter designs which are of utmost importance for small satellites. The advantages of using a micro-ORC power generation system in space instead of a conventional steam Rankine cycle are lower turbine rotational speeds, larger turbine designs, lower freezing temperatures and the organic fluid can act as lubricant [10,12,16]. These advantages reduce the system maintenance required for ORC systems to once per year, for current terrestrial applications [17]. This could be extended to a few years to meet the operational life time of a small satellite. Drawbacks of a micro-ORC system include a lack of space heritage and reduction in reliability due to the ORC system having more moving parts than the PV-battery system, as well as potential transient inertial effects during start-up and shutdown, leakages, cooling of components, micro-gravity operation, and large radiators [10,18,19]. Additionally,

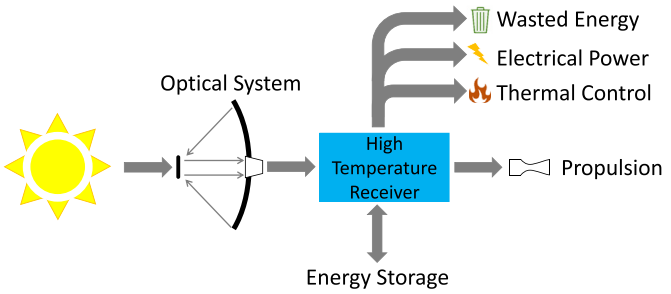

Fig. 1. Schematic of the proposed integrated solar thermal system.

at the low electrical power output considered in this paper ultra-high rotational speeds of more than 500krpm are possible even when using organic working fluids [6].

Research on micro-ORC systems, from a few Watts to 2 kW, has focused on solar thermal and waste energy power generation in portable electronic devices, miniature robotics, automotive industry, and remote off-grid applications [20–23]. However, little is known on the topic of micro-ORC systems, especially for small satellite applications, and investigations have often neglected the sizing of the components such as the turbine and heat exchangers [13]. Therefore, an investigation into the feasibility of generating power by harvesting energy from a solar thermal propulsion receiver on-board a small satellite is required. The satellite is assumed to be in Low Earth Orbit (LEO) at an altitude of 700 km above the Earth, to simulate a mission with low daylight to eclipse ratio. This study focuses on a micro-ORC system that meets the manufacturing and operational constraints while still conforming to the performance requirements. The feasibility is conducted by using a system design methodology comprising a thermodynamic analysis of the micro-ORC system with no pressure drops, where then the heat exchangers are sized and the micro-ORC is re-analysed with the calculated pressure drops. The design approach is combined to a genetic algorithm for the optimal exploration of the design space to minimise the total system volume while meeting the thermal energy storage capacity requirement. A meanline model is used to determine the turbine efficiency of the optimal configuration.

2. System description

A schematic of the proposed system is shown in Fig. 2a. Fig. 2b shows the related thermodynamic cycle in the temperature-entropy diagram of the micro-ORC system. For this study, only superheated regenerative ORC configurations are investigated. The power generation system can be split up into three major parts: 1) the optical system, 2) the high-temperature receiver, and 3) the ORC system. The propulsion system is not analysed in this study.

The optical system consists of a primary mirror, a flat plate secondary mirror and fibre optic cables, as shown in Fig. 3. A parabolic dish was chosen, as the primary concentrator, which concentrates solar radiation onto the secondary mirror, because it can achieve higher concentration ratios than both spherical mirrors and Fresnel lenses or mirrors, which suffer from spherical or chromatic aberration [24]. A non-concentrating flat plate secondary mirror was included as it increases the ease of optical fibre placement and reduces the length of the optical fibre cables required between the concentrator and the receiver, therefore making the design more compact [25]. A flat plate mirror is also simpler and easier to manufacture over improving the performance compared to concentrating secondary mirrors. The optical fibre bundle is made up of a number of individual cables. The diameter of the bundle can be determined based on the number of rings as defined by Fig. 3. The core represents the central optical fibre cable. Fibre optic cables have been included in the design instead of directly focusing solar radiation onto the receiver to reduce the pointing accuracy required and decouple the concentrator and receiver position. This is also a requirement from the propulsion side such that the concentrator position does not constrain the satellite manoeuvring direction. Additionally, they provide the system with the potential to reduce the overall mass by replacing a single large mirror with multiple smaller ones [25]. Disadvantages of the selected optical configuration include decreased end-to-end power efficiency, increased complexity and storage integration challenges.

The solar radiation collected by the receiver superheats the working fluid that is passed through the working fluid tubing coiled inside the insulation of the receiver, illustrated in Fig. 4a, This acts as the evaporator of the micro-ORC system. Near- and far-term high-temperature materials that are suitable to function as receivers for STP applications are silicon and boron respectively [26]. Silicon has been selected as the receiver material and heat source for this work since it is cheaper, more abundant, and a more mature (near-term) material compared to Boron. The receiver is assumed to be cylindrical and is made up of a silicon phase change material (PCM), a boron nitride container, and uses carbon bonded carbon fibre (CBCF) as the insulation material. The receiver also includes a rhenium coating for oxidation protection. The aperture diameter of the receiver is designed to accommodate all the optical fibre bundles entering the receiver, which are part of the optical system. By using a PCM the receiver is able to act as a latent heat energy storage system [26]. Advantages of using a latent heat storage system are relatively constant operating temperatures and high energy storage density, which are attractive qualities for ORC systems and small satellites. The thermal energy stored is crucial to ensure continuous electrical power generation during eclipse periods, therefore not limiting the operations of the small satellite during orbit. Challenges include thermal stresses, radiation losses, and containment of the phase change material. The inclusion of a heat transfer loop between the high-temperature receiver and working fluid was discarded. This was because it would decrease the system efficiency due to the addition of another pump, as well as increase the complexity and therefore reduce the system's reliability. This work, therefore, investigates the possibility of directly embedding the working fluid tubing inside the receiver's insulation, such that the maximum temperature exposed to the working fluid tubing is 20K less than the thermal stability limit of the fluid. The temperature is controlled by placing the working fluid tubing inside the insulation material away from the outer container wall. The distance is calculated based off the receiver's maximum expected temperature, which is equivalent to the melting temperature of the PCM.

The condenser radiates heat to space to condense the working fluid. It is made up of several circular channels, a honeycomb support structure, and two thin flat sheets of aluminium on the top and bottom, referred to as fins, as shown in Fig. 4b. A regenerator is included before the condenser to improve the efficiency of the ORC system. It also reduces the heat transfer surface area of the receiver and condenser at the expense of increased complexity and mass as well as reduced reliability. The regenerator is assumed to be a cross-flow plate-fin heat exchanger (HX) with rectangular channels, depicted in Fig. 4c, due to its compactness, lightweight, and ability to operate at high temperatures. The hot vapour exiting the turbine enters the cross-flow plate-fin HX on the hot side and the cold liquid fluid from the pump enters on the cold side, which is perpendicular to the hot flow. A radial inflow turbine is coupled to a

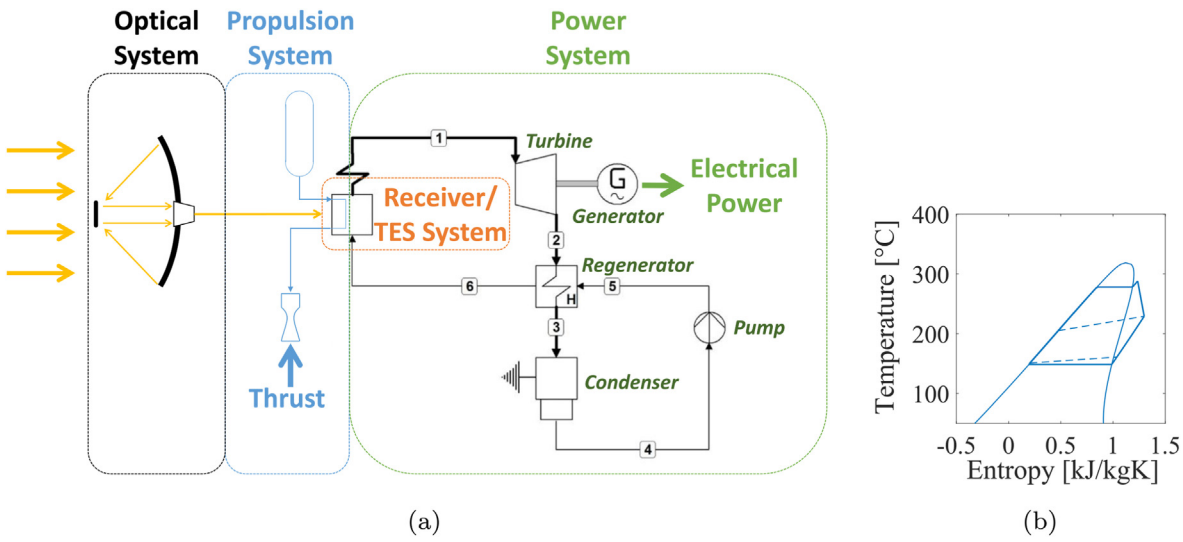

Fig. 2. (a) System schematic and (b) a temperature-entropy diagram of the thermodynamic cycle of the proposed micro-ORC system.

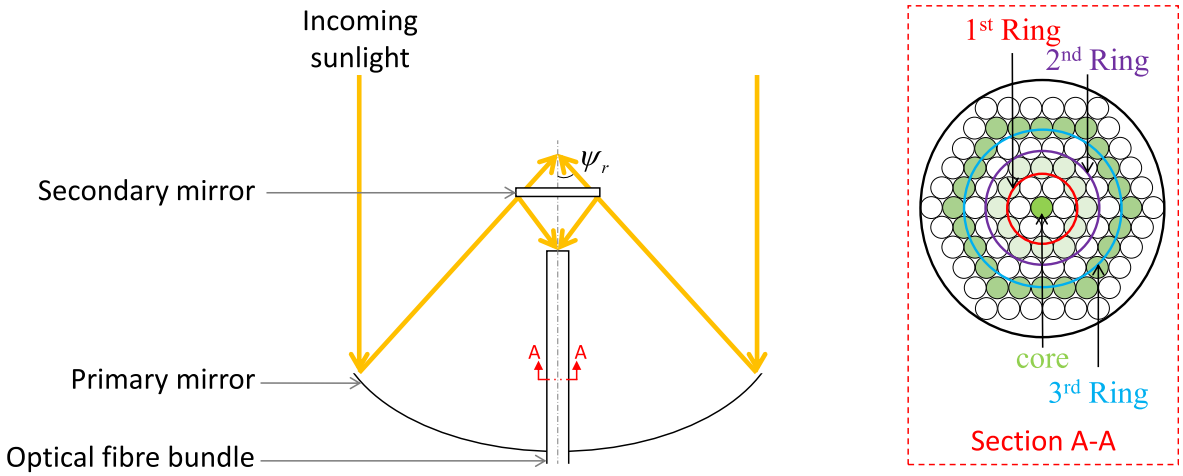

Fig. 3. Schematic view of the optical system, showing the primary and secondary mirror, as well as a cross-sectional view of the optical fibre bundle.

generator to provide on-board electrical power. The selection of this turbine was mainly due to its high power density, comparatively higher efficiency for low power output capacity, and compactness, which are critical aspects for small satellite subsystems.

3. Model description

In this section, the modelling of the system is described, and the sizing method of each component shown in Fig. 2a is discussed. This provides insight into the volume and mass distribution of the system, which is important for satellite design and to determine feasibility.

3.1. Optical system

A critical design aspect of the optical system is the volume required to store the system on-board the satellite during launch, referred to as the stowed volume. Determining the stowed volume of the optical system is difficult without a full design of the concentrating and deployment system. Three concentrator designs are considered in this study: i) a rigid-fixed concentrator, ii) a rigid-deployable concentrator and iii) an inflatable-deployable concentrator design. The total volume of a rigid-fixed design is taken as the volume of a cylinder with the diameter equal to the primary concentrator and the height equal to the distance between the primary dish and secondary mirror plus the thickness of the secondary mirror. The stowed volume of the optical system is assumed to be a percentage of the rigid-fixed design volume with the same primary dish diameter. Parabolic dish designs for the three cases were taken from Refs. [27] and the stowed volume fraction of each system was determined to be 100% for the fixed-rigid design, 25% for the deployable-rigid design and 1% for the inflatable design. An inflatable design was used in the optimisation and the concentrator and support areal densities are assumed to be 1 and 1.5 kg/m^2 respectively [25,26]. The effect of selecting a non-inflatable design type is discussed in Section 5.2 by conducting a one-at-a-time sensitivity analysis on varying the stowed volume fraction input and concentrator areal density.

The total input power of the optical system, $\dot{Q}_{in}$, is determined using Equation (1) [28],

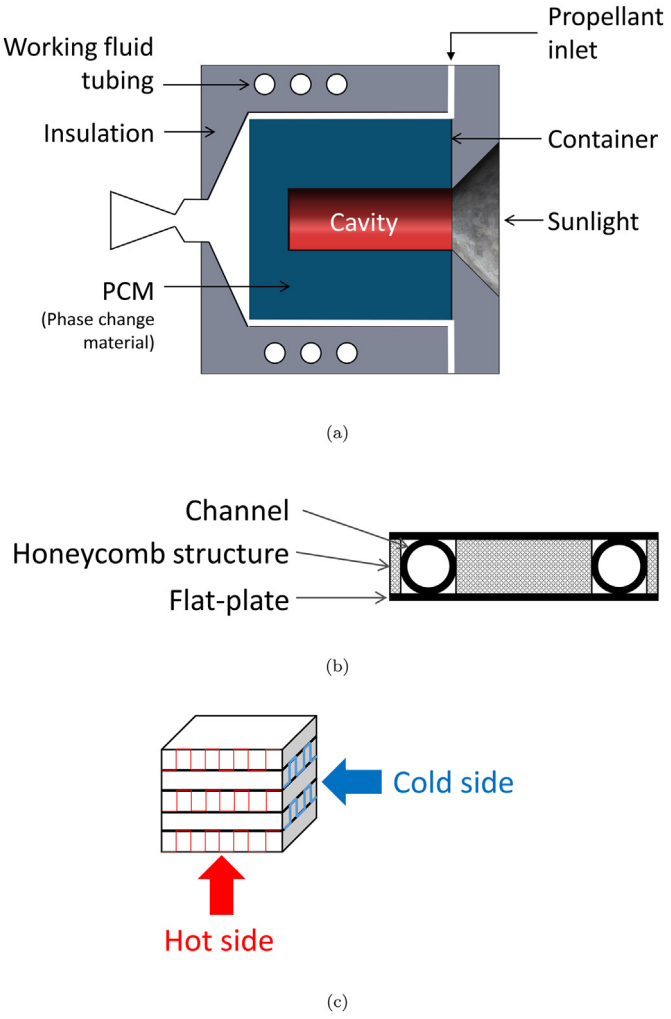

Fig. 4. Schematic representation of the micro-ORC heat exchangers: (a) the receiver, (b) the condenser, and (c) the regenerator.

$$\dot{Q}_{in} = \eta_{op} S A_{op} \left(1 - b_f\right) \tag{1}$$

where the solar flux, S, is assumed to be 1350W/m^2, b_f is the shadow factor (fraction of area of the primary mirror covered by the secondary mirror's shadow), and A_{op} which is the area of the primary mirror times the number of concentrators. The optical efficiency, η_{op}, combines the efficiency of the optical fibre (transmission (90%), Fresnel efficiency (96.5%) and bundle packaging factor) and the primary dish and secondary mirror (reflectivity of the mirrors (90%) and intercept factors (96%)) [29]. The bundle packaging factor, BPF, is defined as the number of optical fibres, N_f, times the area of the one fibre, A_f divided by the bundle area, A_b,

$$\mathrm{BPF} = N_f A_f \big/ A_b. \tag{2}$$

3.2. Receiver

A one-dimensional steady-state radial analysis using a temperature-dependent thermal conductivity and shell thickness method [30] is used to determine the radiation losses through the insulation of the receiver as well as the position of the working fluid tubing (Fig. 4a). The radiation loss through the aperture and the absorption losses of the receiver are also included. From the conservation of energy, an estimated discharge time can be computed during an eclipse if there is adequate energy storage, Equation 3

$$t_{dis} = \frac{M_{pcm} L}{\dot{Q}_o + \dot{Q}_{loss}}, \tag{3}$$

where m_{pcm} is the mass of the PCM, L is the latent heat of the PCM, $\dot{Q}_o$ is the thermal power required for the ORC system, and $\dot{Q}_{loss}$ account for the radiation and absorption losses. The receiver is assumed to act as a lumped-capacity thermal mass with no temperature distribution; this is only valid for low Biot numbers ($\ll 1$) [31]. Therefore this results in a preliminary analysis that requires future in-depth analysis to more accurately determine the coupled convective heat transfer between the PCM, insulation, and the working fluid, as well as the solar flux input. Furthermore, analytical and experimental investigations into the thermal cycling and expansion of the PCM and long exposure between the PCM and its container are required. The expansion of silicon during freezing was not considered in this study. However, it has been found that by reducing the fill factor of the PCM by 80%, the container damage due to the expansion can be mitigated [26]. The volume and mass of the receiver are found based on its described geometry depicted in Fig. 4a, assuming that the length of the inner cavity of the receiver is 80% of the total length of the phase change material.

3.3. ORC modelling

Fig. 5 shows the flowchart of the design method implemented in determining the ORC sizing. First, a steady-state thermodynamic analysis of the ORC system has been carried out using an in-house Matlab code based on the work of [32], assuming no pressure drops through the heat exchangers (HXs). Fluid thermophysical properties are determined by integrating the code with the software library Fluidprop [33]. If the constraints are met, then the HXs are sized and pressure loss calculated as presented in Fig. 5. Thereafter, if the results are within the constraints an updated thermodynamic analysis is conducted incorporating the HX pressure losses. The constraints that result in an infeasible design are described in Section 4.2. Each HX has been discretised to evaluate the one-dimensional local heat transfer coefficient and pressure drop in the single-phase and two-phase flow regions using the models and methods described in Table 1. The mass and volume of the HXs are found based on the geometries described in Fig. 4. Thin-walled pressure vessel and plate fin thickness [34] calculations are performed to ensure structural integrity of the HXs. A safety factor of 2 and 4 [35] are used for the aluminium condenser channel and boron nitride evaporator tubing based on the yield stress and maximum expected pressure. The minimum condenser channel is set to 1 mm in this paper due to machinability and deployability concerns. The regenerator is assumed to be manufactured out of Inconel 617 with its temperature dependant allowable yield stress provided by Ref. [36].

In the evaporator, the high operating wall temperatures could result in low/high-quality critical heat flux (CHF) regimes. The CHF quality is determined using the method proposed by Ref. [45]. If the CHF quality is low, boiling is split into Inverted Annular Flow Boiling (IAFB) and Dispersed Flow Film Boiling (DFFB) regimes. Dryout at high qualities will result in DFFB being present after saturated boiling flow. Both of these flow types, can considerably reduce the heat transfer coefficient and thus increase the evaporator tubing length required for sufficient heat transfer.

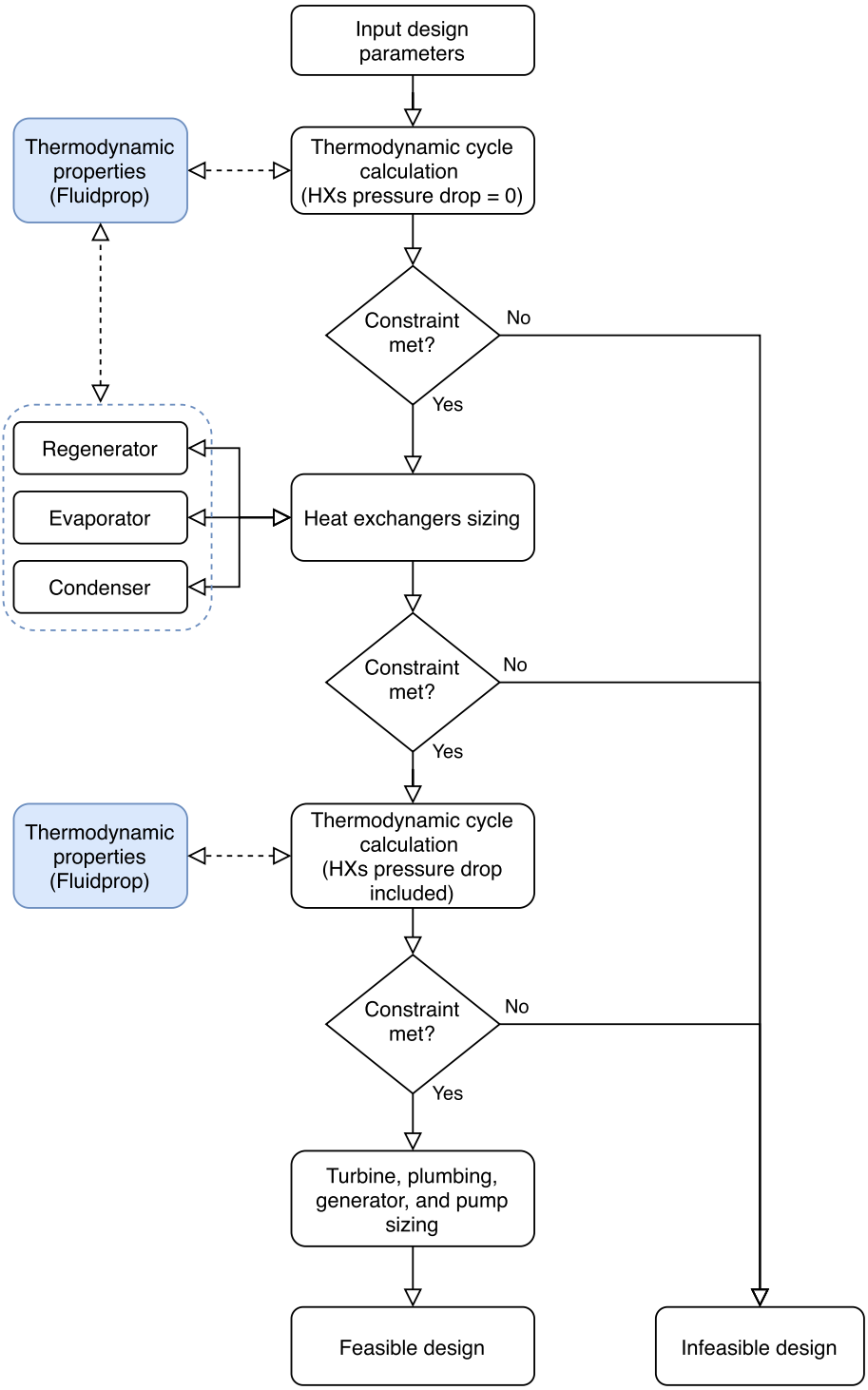

Fig. 5. Flowchart illustrating the implementation of the design of the micro-ORC system. Dashed lines represent the coupling of the Matlab code with Fluidprop to determine the thermophysical properties of the working fluid.

The radial inflow turbine geometry was analysed based on a meanline model similar to that proposed in Ref. [32]. It is assumed that the change in kinetic energy is negligible between the turbine inlet and outlet, that the flow in the stator is isentropic, and the deviation angle at both stator and rotor exit is null. Although, in reality these assumptions may affect the results, it is assumed the changes generated by these effects can be neglected for simplicity of the model as the trend should be correct [32]. A conservative value has been taken for the mass and volume of the turbine by assuming it is a solid disk with a diameter equivalent to the stator and the length equal to the axial length of the turbine. The turbine is assumed to be manufactured out of titanium due to manufacturability and high operating temperatures.

The remaining components of the system that require sizing are the pump, generator, and plumbing. The plumbing consists of circular tubing connecting the ORC components to each other. Each

Table 1
Models and methods implemented to determine the heat transfer coefficient and pressure drop in the heat exchangers.

Component	Flow type	Method/Model	Reference
Regenerator	Single-phase[a]	The plate-fin rating model and ε-NTU method are used with frictional factors and Nusselt numbers provided in Table 2 for rectangular channels.	[37]
Evaporator	Single phase[a]	Frictional factors and Nusselt numbers used are provided in Table 2 for circular channels.	
	Two-phase[b,c] (saturated)	Universal method used to predict saturated flow boiling heat transfer coefficient and two-phase frictional pressure drop for mini-channels.	[38–40]
	IAFB and DFFB	Empirical correlations	[41,42]
Condenser	Single phase[a]	Frictional factors and Nusselt numbers used are provided in Table 2 for circular channels.	
	Two-phase[b,c] (saturated)	Universal method used to predict saturated flow condensing heat transfer coefficient and two-phase frictional pressure drop for mini-channels.	[43,44]

[a] Only the frictional effects are considered for single phase flow pressure drop calculations.
[b] Accelerational pressure drop is negative for condensing flow and positive for positive for boiling flow.
[c] Gravitational pressure drop is neglected in two-phase flow due to operation in micro-gravity.

Table 2
Friction factor and Nusselt number correlations used in the heat exchangers.

Equations	Reference
Laminar developing flow: Rectangular channel[a]	
$f_{app} = \frac{1}{\mathrm{Re}}\left[3.44(x^+)^{-0.5} + \frac{K(\infty)/(4x^+) + fRe - 3.44(x^+)^{-0.5}}{1 + C(x^+)^{-2}}\right]$	[46]
$\mathrm{Nu} = [0.277 - 0.152e^{(-38.6x^*)}]^{-1}$	[47]
Laminar fully developed flow: Rectangular channel	
$f = \frac{24}{\mathrm{Re}}(1 - 1.35553\beta + 1.9437\beta^2 - 1.7012\beta^3 + 0.9564\beta^4 - 0.2537\beta^5)$	[46,47]
$\mathrm{Nu} = 8.235(1 - 2.0421\beta + 3.0853\beta^2 - 2.4765\beta^3 + 1.0578\beta^4 - 0.1861\beta^5)$	[46,48]
Laminar developing flow: Circular channel	
$f = \frac{16}{\mathrm{Re}}$	[30]
$\mathrm{Nu} = 4.364$	[30]
Turbulent fully developed flow: Rectangular channel[b]	
$f = \frac{1}{4}\frac{1}{(0.790\ln(\mathrm{Re}) - 1.64)^2}$	[49]
Turbulent fully developed flow: Circular channel	
$f = \frac{0.079}{\mathrm{Re}^{0.25}}, 2000 \le \mathrm{Re} < 20000, f = \frac{0.046}{\mathrm{Re}^{0.2}}, \mathrm{Re} \ge 20000$	[39,44]
$\mathrm{Nu} = \frac{\frac{f}{2}(\mathrm{Re} - 1000)\mathrm{Pr}}{1 + 12.7\left(\sqrt{\frac{f}{2}}(\mathrm{Pr}^{\frac{2}{3}} - 1)\right)}$	[50]

[a] Constants $K(\infty)$, fRe, and C in the apparent friction factor can be found in [47].
[b] The Gnielinski equation [50] can be used to determine the Nusselt number for rectangular ducts as it gives an error $\le$ 9% for rectangular ducts with all four sides heated [47].

section of tubing has a length equivalent to three times the largest characteristic length of the component it provides an outlet for. The tubing material is assumed to be titanium and aluminium for vapour and liquid flows respectively, such that the tubing can withstand the high temperatures and is compatible with the working fluids analysed such as Toluene. Wall thickness is determined based on hoop stresses assuming a safety factor of 3 on the operating pressure [35]. A survey was conducted on available micro-pumps and generators suitable for a 200 W micro-ORC. The result of the micro-pump study shows that the volume of the micro-pump remained similar for different differential pressure. Therefore, for simplicity the pump volume and mass are equal to the maximum values found from the survey rounded up to 0.001 m^3 and 1.5 kg respectively to be more conservative. Linear relationships were derived to relate the mass ($M_g = a\dot{W}_{net} + b$) and volume ($V_g = c\dot{W}_{net} + d$) of the generator to the net power output $\dot{W}_{net}$, where the coefficients a, b, c, and d are defined as 1.8 kg/kW, 2.718 kg, 2×10^{-6} m^3/W, and 7×10^{-5} m^3.

3.4. System model validation

Validations on determining the size and performance of the micro-ORC system have been conducted and presented in Table 3. Most components are validated with given data in terms of mass which can be equated to volume based on geometry and density. All component validations fall within the acceptable threshold of 5%, except for the volume of the optical system and the overall heat transfer and conductance of the regenerator.

The rigid volume of the concentrator was found to have a large deviation of 17% due to the lack of data on the design of the 0.5 m dish from Ref. [27] as well as the assumption that this study assumes the rigid volume of the optical system is equivalent to a cylinder. This deviation is assumed acceptable for this analysis as it provides a more conservative approach taken in this work, especially as the pressurisation system required to inflate the optical system is not modelled. The regenerator model was validated against the commercially available ASPEN Exchanger Design and Rating [52] software. Both the hot and cold side of the regenerator were assumed to use Toluene as the working fluid, 5 bar pressure, 10 kg/s mass flow rate, 20 layers, and a fin height of 8.9 mm. The hot

Table 3
Model validations.

System	Parameter	Unit	Reference Value	Reference	This Study	Difference [%]
Receiver						
	PCM Mass	[kg]	66.8	[26]	67.3	0.7
	Container Mass	[kg]	9.4	[26]	9.3	1.1
	Coating Mass	[kg]	62.6	[26]	52.4	0.4
	Total Mass	[kg]	128.8	[26]	129	0.2
Optical						
	Focal Length	[mm]	33.7	[31]	33.8	0.3
	Mass	[kg]	15	[31]	14.78	1.5
	Rigid Volume	[m^3]	0.05	[27]	0.0593	17
Regenerator						
	Overall Heat Transfer	[kW]	277.2	ASPEN EDR	249.61	10.47
	UA Value	[kW/K]	7.9	ASPEN EDR	7.117	10.42
	Temperature - Hot Side	[K]	457.58	ASPEN EDR	459.568	0.43
	Temperature - Cold Side	[K]	436.25	ASPEN EDR	434.963	0.3
	Pressure - Hot Side	[bar]	4.945	ASPEN EDR	4.802	2.92
	Pressure - Cold Side	[bar]	4.999	ASPEN EDR	4.997	0.05
	Empty Mass	[kg]	106.1	ASPEN EDR	100.6	5.32
	Operating Mass	[kg]	165.5	ASPEN EDR	159.3	3.82
Condenser						
	Average Area	[m^2]	5.24	[51]	5.16	1.4
	Average Mass	[kg]	3.76	[51]	3.67	2.9

and cold side temperatures were 200°C and 150° Crespectively. The hot side length, fin thickness, and fin frequency were 0.418 m, 0.2 mm and 787 fins/m, whereas the cold side was 0.485 m, 0.41 mm and 236 fins/m. A maximum percentage error of 10.5% for the overall heat transfer and conductance (UA value) was found. Higher tolerance for these values is acceptable with deviations as high as 30% experienced in literature.

Table 4 provides the sample size, the mean absolute error (MAE) and the percentage of results predicted within 30% and 50% of the experimental results, θ and ζ respectively. The predicted results are obtained using the correlation derived by Refs. [40,44] for saturated boiling and condensing frictional pressure drop respectively, and the experimental data points are from Ref. [53] for boiling flow and [54] for condensing flow. For the saturated two-phase flow heat transfer coefficient, predicted values are obtained using [39,43] for boiling and condensing flow, respectively. Experimental data are provided by Ref. [55] for boiling flow and [56] for condensing flow. Based on the results, the use of the saturated boiling and condensing heat transfer correlations is deemed adequate as the predicted results fall mostly within 30% of the experimental. The frictional pressure gradient has a larger deviation, however, mostly the large discrepancies occur at low values (less than 5 kPa/m) and therefore deemed adequate for this preliminary analysis.

4. Design methodology

The focus of the paper is on the feasibility of micro-ORCs for space applications. An optimisation using a genetic algorithm to minimise the micro-ORC system volume is described in this section. Before the system is analysed and sized, it is necessary to ensure suitable heat transfer correlations are used. A concern for the proposed system, is the possibility of the working fluid in the evaporator to operate in the IAFB and DFFB regimes, as mentioned in Section 3.3. Therefore, an investigation into the boiling flow regime of the evaporator is warranted due to the high operating temperatures expected in the receiver. Finally, a set of suitable turbine loss models are discussed and validated so that the turbine performance of the optimal design can be estimated. Fig. 6 provides a flowchart summarising the three main investigations conducted in this work.

4.1. Critical heat flux analysis

To the authors' knowledge, no ORC optimisation study has included the effects of boiling flow in the IAFB and DFFB regimes. A number of IAFB and DFFB empirical correlations provided in Ref. [41,42] are analysed to determine the most suitable correlations for this study. This analysis includes comparing the empirical correlations with experimental data based using R134a [57] and water [58,59]. A local sensitivity analysis, using the one-at-a-time (OAT) technique was also conducted on the two-phase boiling heat transfer coefficient to minimise this uncertainty, due to a lack of experimental validation of the correlations and working fluid considered in this study. This sensitivity analysis was conducted on various operating pressures (1, 10, and 20 bar), tube diameters (1, 2, 3, and 6 mm), surface wall temperatures (500, 550, and 650 K) and mass flow rates (1, 5, and 10 g/s), that are expected to occur during the optimisation study, with the baseline parameters underlined. The working fluid was taken as Toluene and the maximum (bulk) temperature was constrained to 10K above its saturation

Table 4
Saturated boiling and condensing flow heat transfer coefficient and frictional pressure gradient verification.

	Saturated Boiling		Saturated Condensation	
	Heat transfer coefficient	Frictional pressure gradient	Heat transfer coefficient	Frictional pressure gradient
Sample size	9	645	45	36
MAE [%]	11.37	24.56	17.35	23.84
θ [%]	100.00	82.02	91.11	69.44
ζ [%]	100.00	92.25	100.00	88.89

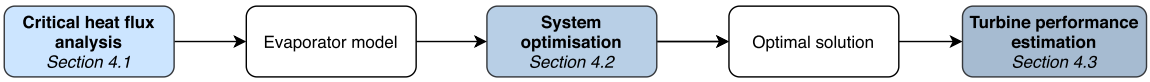

Fig. 6. Flowchart showing the three main investigations covered in this paper and their interdependency.

temperature. The effect of various heat transfer coefficients on the system was also investigated by assuming constant heat transfer coefficient values in the system model. The results are provided in Section 5.1. The selected IAFB and DFFB empirical correlations were then used in the evaporator model in the optimisation study (discussed in the next section) to determine the heat transfer coefficient if these flow regimes were experienced.

4.2. System optimisation

An investigation into the feasibility of a micro-ORC system in terms of volume has been conducted. Reducing the volume and mass are both crucial for small satellite subsystems. However, these variables are proportional to each other and therefore only one variable needs to be considered in the optimisation. System volume was selected as a more appropriate optimisation variable due to the physical concerns regarding integration inside the launch vehicle, especially of large components such as the concentrators. Only superheated configurations with regeneration are analysed, as illustrated in Fig. 2b. The analysis is performed using a single-objective genetic algorithm (GA) implemented in MATLAB [60] based on the system architecture shown in Fig. 2a. The optimisation process is shown in Fig. 7. Genetic algorithms are common methods used in ORC optimisation studies [61] due to their robustness, however at the expense of higher computational time when compared to other methods such as the direct search and variable metric method.

For this study, the optimisation minimises the objective function, $F(x)$, with respect to the design variables, x, defined in Equation (4),

$$F(x) = \{\mu_1(x)\}^2 + \{\Omega\}^2 \tag{4}$$

where μ_1 is the system volume fraction ($\mu_1 = V_{sys}/V_{sc}$) and Ω is the penalty term. The total volume of the ORC system, V_{sys}, is the summation of the volume of the evaporator, regenerator,

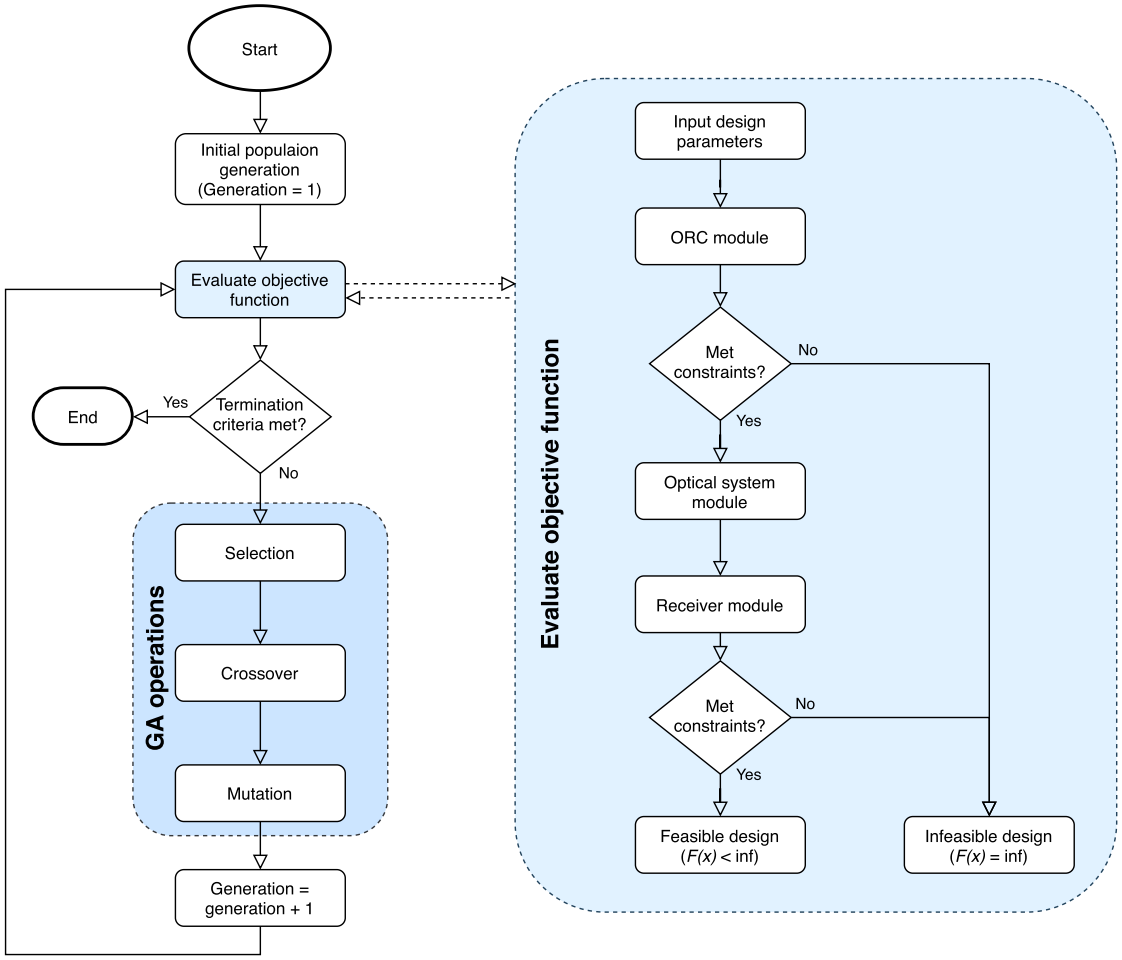

Fig. 7. Flowchart illustrating the optimisation process. Section 3 discusses the component modules used to evaluate the objective function.

condenser, pump, plumbing, and turbine. An additional margin of 20% has been included to account for miscellaneous components such as support structures, interfaces, and control hardware. The total volume of the satellite is denoted by V_{sc} and is determined based on the allowable payload volume inside the standard Evolved Expendable Launch Vehicles (EELV) Secondary Payload Adapter (ESPA). The micro-ORC system is constrained to produce 200 W of electrical power output.

The parabolic penalty method has been used to increase the search domain by relaxing specific system constraints into a penalty term and reduce the risk of non-convex solutions by squaring each term in the objective function [62]. The penalty term is defined as the summation of penalty parameters, P_i,

$$\Omega = \sum_{i=1} P_i(x) \tag{5}$$

where $P_i = \chi/\chi_{\max}$ if $\chi > \chi_{max}$ or $P_i = \chi_{\min}/\chi$ if $\chi < \chi_{\min}$. The parameter χ represents the system constraint that has been relaxed such that the solution is not discarded during the iteration process of the optimisation. In this case, a penalty is given if the fluid velocity in the HXs (regenerator, evaporator, and condenser) falls outside the limits for liquid ($0.5 \leq u_f \leq 5$), vapour ($1 \leq u_v \leq \min[60 \quad 175\rho_v^{-0.43}]$), and two-phase ($1 \leq u_{tp} \leq 183\rho_m^{-0.5}$) flow [63]. Penalties are also given if the mass velocity, Reynolds number (liquid-only, superficial liquid, and superficial vapour), and reduced pressure falls outside the range of validity of the two-phase flow correlations used in the condenser [43] and evaporator [38] models. $\chi_{\min}$ and $\chi_{\max}$ represent the upper and lower feasible bounds of these parameters.

Constraints that result in infeasible solutions that are not passed through the iteration process are provided in Table 5 along with the fixed parameters used in the optimisation. Table 6 defines the 14 design variables, x, used and their corresponding upper and lower limits.

The upper value of the maximum pressure was set to 5% less than the critical pressure of the working fluid and the lower value was set to 1 bar, to explore a broad design space. In terrestrial applications, the minimum cycle pressure of the working fluid has to be greater than atmospheric pressure to avoid air leakage into the system. This is not a concern in this design due to vacuum ambient conditions. However, the lower limit of the minimum cycle pressure was restricted to 0.1 bar to ensure the condenser pressure losses could be overcome. Fin geometry ranges are limited to common values used in plate-fin heat exchanger designs [37]. The length of hot and cold sides of the regenerator was constrained for spacial constraints and to minimise the aspect ratios for structural concerns. A minimum of 2 hot layers was set because the hot channels form the outer part of the regenerator, as shown in Fig. 4c. Further improvement in the regenerator design could be to design the cold layers on the outside to minimise heat loss and extend the length of the hot and cold sides. The diameter of the condenser was limited to the validity range of the condensing heat transfer correlations [43,44]. The minimum number of concentrators was set as 2 for redundancy. The lower bound of the number of fibre rings, as described by Fig. 3, was set to 2 because one ring does not meet the power input requirement. A wide range of receiver geometries was also evaluated to meet the thermal energy storage requirement, to ensure continuous power generation during eclipse periods. The

Table 6
Optimisation design variables and corresponding design range.

	Design Parameter	Unit	Range
x_1	Maximum cycle pressure	bar	1 - 0.95p_{cr}
x_2	Minimum cycle pressure	bar	0.1–5
x_3	Regenerator fin height	mm	0.2–8
x_4	Regenerator fin thickness	mm	0.1–1
x_5	Regenerator fin frequency	fin/m	100–1000
x_6	Regenerator length of hot side	mm	1–100
x_7	Regenerator length of cold side	mm	1–100
x_8	Number of hot layers		2–200
x_9	Condenser diameter	mm	0.2–6
x_{10}	Number of concentrators		2–20
x_{11}	Number of rings (fibre bundle)		2–10
x_{12}	Receiver thickness	mm	1–100
x_{13}	Receiver length	mm	1–100
x_{14}	Receiver insulation thickness	mm	1–500

Table 5
Optimisation constraints and system model parameters.

Constraints			Model parameters		
Rotor blade height:	$b > 0.2$ mm	*	Stator inlet to outlet radius ratio:	$\frac{r_0}{r_1} = 1.3$	†
Regenerator thickness to height ratio:	$\frac{x_5}{x_4} < 1$	*	Stator outlet to rotor inlet radius ratio:	$\frac{r_1}{r_2} = 1.02$	†
Regenerator thickness:	$x_5 \geq \frac{p}{n_{fin}\sigma_{fin}}$	*	Rotor shroud outlet to inlet radius:	$\frac{r_{s,3}}{r_2} = 0.7$	†
Receiver length to evaporator length:	$\frac{L_{rec}}{L_{ev}} \geq 1$	*	Rotor outlet hub to shroud radius ratio:	$\frac{r_{h,3}}{r_{s,3}} = 0.4$	†
Discharge time:	$t_{dis} \geq t_{eclipse}$	†	Absolute flow angle, rotor inlet:	$\alpha_2 = 80^\circ$	†
Min. to max. cycle pressure ratio:	$\frac{x_3}{x_2} < 1$	†	Relative flow angle, rotor exit:	$\beta_3 = 60^\circ$	†
Relative rotor Mach Number:	$M_{2,rl} < 0.85$	†	Axial flow coefficient:	$\varphi = 0.3$	†
Relative flow velocity ratio:	$\frac{w_3}{w_2} > 1.5$	†	Spacecraft volume and mass:	$V_{sc} = 0.3976$ m^3, $M_{sc} = 215$ kg	‡
Regenerator pinch point temperature:	$\Delta T_{pp,rg} \geq 20$	†	Eclipse time:	$t_{eclipse} = 35,29$ minutes	‡
Max. evaporator wall temperature	$T_{wall} = T_{stability} - 20$	†	Isentropic efficiencies:	$\eta_t = 65\%$, $\eta_p = 50\%$, $\eta_g = 100\%$	†
Max. working fluid temperature	$T_{wf} = T_{sat} + 10$	†	Solar flux and Sun half-angle:	$S = 1350$ W/m^2, $\theta = 0.266^\circ$	‡
			Optical fibre efficiency:	$\eta_f = 83.8\%$	*
			Fibre mass per length:	$\bar{L} = 9.95$ g/m	*
			Shadow factor:	$b_f = 0.02$	*
			Electrical power output:	$\dot{Q} = 200$ W	‡

* Manufacturing limit.
† Flow condition.
‡ Satellite mission.

insulation range ensures the working fluid does not exceed its thermal stability limit. It is expected that the MM and MDM scenarios will therefore require larger insulation thickness to meet the thermal stability constraint. For a specific satellite mission, the temperature of the outer layer of the insulation can be constrained to the required spacecraft environment for better thermal control, however, this is not considered in this study.

The optimisation was run for six working fluids Toluene, MM, MDM, D4, D5, and D6, based on the results of [6] as well as the work of [10], to identify the most suitable working fluid for small satellite applications. Working fluids are constrained to fluids that correspond to a Fire Protection Association (NPFA) 704 health rating of less than 4 to minimise the integration risks of a small satellite with the primary payload on-board the launch vehicle. Flammability is less of concern in space due to the absence of oxygen reducing the risk of a fire. However, the flammability of the fluid increases handling costs and launch risks.

The optimisation population size was set to 140, and the termination criterion was set as either a convergence criterion of 10^{-10} or a maximum number of generations of 1000. These values were selected as a compromise between computational speed and accuracy. An initial mutation rate of 0.02 and a crossover probability of 0.7 were used.

4.3. Turbine performance estimation

The turbine efficiency decreases with size. The major reason for this decrease is because the relative aerodynamic losses increase for smaller designs, such as the relative clearance between the blade and shroud gets larger which increases the losses. Generally, during the preliminary design phase, turbine losses are determined using loss model correlations. However, these empirical loss correlations have been developed for large-scale turbines using non-organic fluids and their accuracy for the problem at hand is debatable. There is a lack of experimental testing of micro-radial inflow turbines (micro-RIT), which are necessary to characterise and quantify the associated turbine losses.

To determine an estimation of the losses and provide more realistic preliminary results, this work extends the research conducted by Ref. [64] and uses a set of loss models that were found to be acceptable for small-scale applications (with rotor diameters of 30 mm). These loss models show satisfactory agreement within 5% of the total-to-static efficiency compared with CFD results and 14% compared to experimental data [64]. In this case, we are interested to maximise the total-to-static efficiency, η_{TS}, given by Equation (6),

$$\eta_{TS} = \left[\frac{1}{\eta_{TT}} + \frac{0.5v_3^2}{\Delta W_{is}}\right]^{-1}, \tag{6}$$

$$\eta_{TT} = 1 - \zeta_R \frac{w_3^2}{2\Delta W_{is}} - \zeta_N \frac{v_2^2}{2\Delta W_{is}}\left(\frac{T_3}{T_2}\right), \tag{7}$$

where, η_{TT} is the total-to-total efficiency, v is the absolute velocity, w is the relative velocity and T is the static temperature. The subscripts 2 and 3 refer to the rotor inlet and outlet section. ΔW_{is} is the Eulerian work obtained from the isentropic calculation performed in Stodola [65]. The loss coefficient of the stator, ζ_N, was computed by resorting to the Glassman model complemented by a first-principle loss model for the mixing losses [66]. The rotor loss coefficient ζ_R, can be calculated using Equation (8) and is made up of tip clearance, Δh_{tc}, secondary flow, Δh_{sf}, skin friction, Δh_{fric}, and incidence losses, Δh_{inc},

$$\zeta_R = \frac{h_3 - h_{3,is}}{0.5w_3^2} = \frac{\Delta h_{loss}}{0.5w_3^2}. \tag{8}$$

A large concern with small scale turbomachinery is the tip-leakage loss due the relatively high tip gap to blade span ratio resulting from manufacturing and safety constraints. Here, the associated loss is calculated according to Equation (9) [67],

$$\Delta h_{tc} = 0.4\frac{tc}{b_2}v_{2,u}^2. \tag{9}$$

where tc is the tip clearance and b_2 is the rotor inlet blade height. Equation (10) [67–69] determines the losses inside the blade passage such as secondary flow loss and skin friction loss,

$$\Delta h_p = \Delta h_f + \Delta h_{sf} = \frac{1}{2}\left(c_{f,c}, \frac{L_{hyd}}{D_{hyd}}\overline{w}^2 + \frac{r_2 v_2^2}{r_c Z}\right), \tag{10}$$

where, r_c is the radius of curvature and Z is the number of rotor blades.

The average velocity $\overline{w}$ is defined as $\overline{w} = 0.5[w_2 + 0.5(w_{3,sh} + w_{3,hb})]$ [70], the modified friction coefficient, $c'_{f,c}$ is determined by the correlation proposed by Ref. [71] shown in Equation (11) to account for the effects of curvature in the turbine. The friction coefficient, $c_{f,c}$ is determined using Equation (12) [72] and the Fanning friction factor f is calculated as $f = 16/\mathrm{Re}_{av}$ if laminar flow and the Colebrook-White correlation if turbulent flow [73],

$$c'_{f,c} = c_{f,c}\left[\mathrm{Re}\left(\frac{D_2}{2r_c}\right)^2\right]^{0.05}, \tag{11}$$

$$c_{f,c} = f\left[1 + 0.075\mathrm{Re}^{0.25}\sqrt{D_{hyd}/(2r_c)}\right]. \tag{12}$$

The incidence losses can be determined using Equation (13) [74] and the losses caused by the rotor outlet kinetic energy referred to as the exit losses is given by Equation (14) [64],

$$\Delta h_{inc} = 0.5w_{2,u}^2, \tag{13}$$

$$\Delta h_{ee} = 0.5v_3^2. \tag{14}$$

The predictive capability of the loss model for small-scale applications was verified by a test case example. The turbine design used as the test case is the ORCHID mini-turbine [66] that uses MM as the working fluid; additional inputs are given in Table 7. Results

Table 7
ORCHID mini-turbine test case input parameters.

Parameter	ORCHID Test Case	Micro-turbine design
Working fluid	MM	Toluene
Mass flow rate [kg/s]	0.132	0.00405
Total inlet temperature [°C]	300.00	287.99
Total inlet pressure [bar]	18.10	24.58
Static exit pressure [bar]	0.443	3.211
Rotational speed [krm]	98.00	771.62
Inlet blade height [mm]	2	0.266
Tip clearance [mm]	0.1	0.075
Inlet blade height to diameter ratio	0.02874	0.03830
Reaction degree	0.37	0.4
In/out stator diameter ratio	1.3	1.3
In/out clearance diameter ratio	1.04	1.03
In/out mean rotor diameter ratio	1.79	2.0

Table 8
Verification of the total-to-static efficiency of the implemented loss model of the ORCHID turbine.

	CFD [66]	Baines [75]	Present model
η_{TS} [%]	84.00	81.06	78.84
Difference [%]	6.34	2.78	–

are compared with the Baines model [75] using the STODOLA software [65]. For simplicity, the average velocity in Equation (10) is taken as the average of the inlet and outlet of the rotor. The results of the verification analysis performed on the ORCHID turbine are shown in Table 8. The total-to-static efficiency using the empirical loss models defined in this study is found to be within 3% of the model described by Baines and 6.5% of the CFD results. The implemented model is shown to provide a conservative value of the total-to-static efficiency.

Table 7 provides the input values used to determine the turbine efficiency of a micro-turbine design. The turbine efficiency is varied from 45 to 65% in a OAT sensitivity analysis to determine the impact of turbine efficiency on the system feasibility.

5. Results and discussion

5.1. Critical heat flux results

Table 9 provides the indexing of the existing IAFB and DFFB correlations used in the CHF analysis. The table also provides the results of the empirical correlations compared with experimental data, to identify which empirical correlations are the most suitable. The results indicate that the correlations that perform the closest with the experimental data in terms of MAE, θ, and ζ are the models proposed by Breen and Westwater (Index 3), and Bromley based on either using the vapour (Index 1) or vapour film temperature (Index 2) for the IAFB regime. The closest performing DFFB correlations are the Bishop (Index 9), Tong (Index 13), and Slaughterbeck (Index 14) correlations.

Table 9
Indexing of IAFB and DFFB correlations analysed and assessment of correlations against experimental tests. Correlations are defined in Ref. [41,42].

No.	Empirical Correlations	MAE [%]	θ [%]	ζ [%]
IAFB: Sample size 325				
1	Bromley using T_v (1952, 1953)	29.77	46	97
2	Bromley using T_{vf} (1952, 1953)	28.17	59	99
3	Breen and Westwater (1962)	22.37	70	100
4	Berenson (1961)	45.08	15	59
5	Wallis and Coiller (1980)	> 100	0	0
6	Bailey (1972)	28.10	70	85
7	Andersen (1976)	> 100	0	0
8	Ellion (1954)	71.87	2	4
9	Collier (1980)	77.00	2	4
10	Siviour and Ede (1970)	40.42	23	70
DFFB: Sample size 25				
1	Polomik, 1 (1961)	> 100	0	8
2	Polomik, 2 (1961)	33.05	48	72
3	Polomik, 3 (1961)	31.65	48	76
4	Polomik, 1 (1967)	32.67	52	68
5	Polomik, 2 (1967)	60.73	24	44
6	Collier (1962)	99.85	0	0
7	Bishop, 1 (1965)	46.09	40	52
8	Bishop, 2 (1965)	29.45	52	72
9	Bishop, 3 (1965)	19.15	80	100
10	Lee (1970)	99.79	0	0
11	Miropolskiy (1963)	87.40	4	20
12	Brevi (1969)	100.00	0	0
13	Tong (1965)	26.91	52	96
14	Slaughterbeck (1973)	22.57	60	100
15	Groeneveld (1969)	92.42	4	16
16	Mattson (1974)	99.17	0	0

The Bishop (Index 9) DFFB correlation was selected for use in the optimisation study because it is the best performing correlation against the experimental data, illustrated in Table 9. Although, the Breen and Westwater (Index 3) correlation provides the most comparable values with the experimental data, the Bromley (Index 2) correlation was selected for use in the optimisation study. Fig. 8a indicates that for the operating conditions expected in this optimisation study the Bromley (Index 2) and Breen and Westwater (Index 3) correlations provide similar heat transfer coefficients, thus making it acceptable to select the Bromley (Index 2) correlation. By using the Bromley correlation we reduce the dependency of the film boiling heat transfer coefficient on the surface tension, which was uncertain for D5, D6 and MDM siloxanes under investigation. It was found that the diameter has the most significant influence on the DFFB heat transfer coefficient and that most IAFB correlations are not affected by the mass flow rate, as shown in Fig. 8. During this sensitivity analysis, the radiation heat transfer coefficient accounted for a maximum of 6% of the total heat transfer coefficient for both the Bromley and the Bishop correlations, assuming a wall and liquid emissivity of 0.95 and 0.6 respectively.

The results in Table 10, showing the effect of heat transfer coefficients on the ORC system, indicate as expected an increase in evaporator length and volume with decreasing heat transfer coefficient. However, the ORC volume and thermal efficiency are not significantly affected, and therefore the use of the selected IAFB and DFFB correlations in the optimisation is assumed to be satisfactory for the purposes of determining a preliminary design of the proposed system. The small effect on the ORC volume is also due to the rest of the ORC system components, such as the concentrator, condenser and regenerator, remaining the same for this analysis.

5.2. System optimisation results

Table 11 shows the design input parameters for the optimal solutions of all the working fluid scenarios that can meet the discharge time required to operate continuously during the eclipse period. The results illustrate that the length of the cold side of the regenerator reaches the upper bound of the given range. Extending the upper limit of the cold side length, results in an increase in regenerator geometry and thermal efficiency of the system by 1–2%. If the design requires a higher discharge time then a larger receiver is needed. At discharge time requirements of more than three times that specified in this optimisation, a larger optical system is also needed to meet the energy input required to obtain the thermal storage capacity.

The volume and mass of all the components for the various working fluids are provided in Fig. 9. The critical component of the system is the concentrator has it has the largest stowed volume and mass, for the Toluene case they occupy 11.5% and 13.25% of the total allowable spacecraft volume and mass respectively.

Inflatable concentrators are necessary for the feasibility of micro-ORC systems as deployable rigid concentrators significantly exceed the spacecraft volume for the input power requirement, as depicted in Fig. 10a. For example, the concentrator stowed volume fraction increases from 11.5% to 57.5% when changing the concentrator storage volume from 1% to 5%. Additionally, changing the design from inflatable to rigid the concentrator mass fraction increases from 13.25% to 31.04%. Fig. 10b illustrates the mass saving potential of inflatable designs, although this sensitivity analysis does not include the mass of the pressurisation system needed to inflate the optical system.

The receiver and condenser are the next largest components. These components, together with the generator, make up the

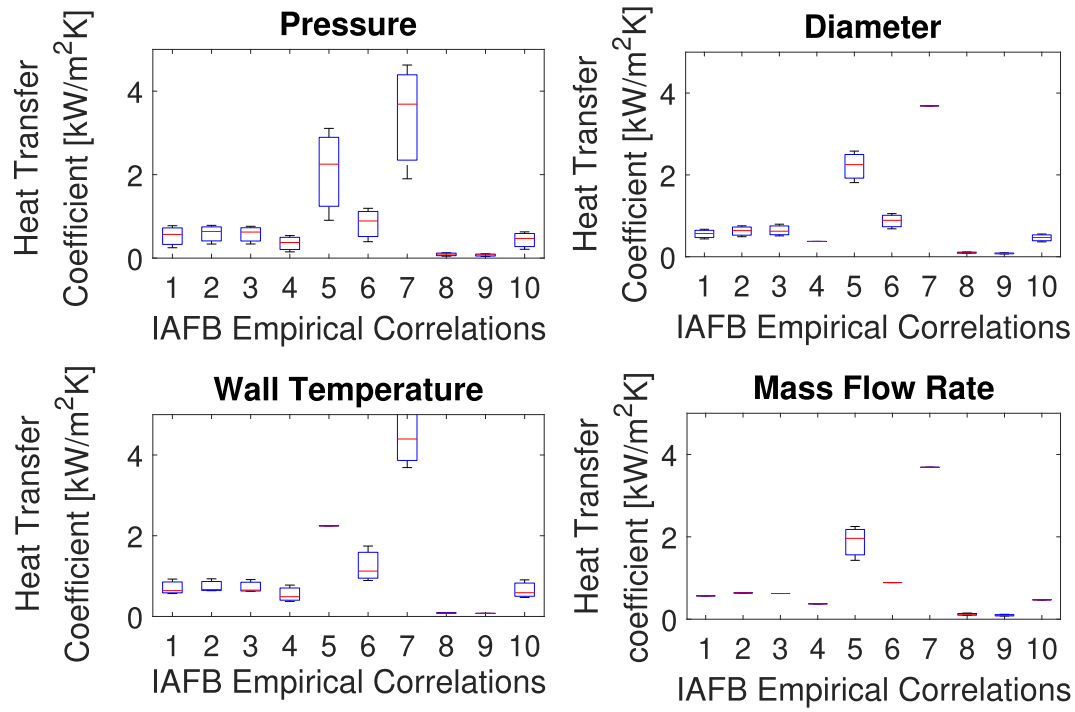

(a)

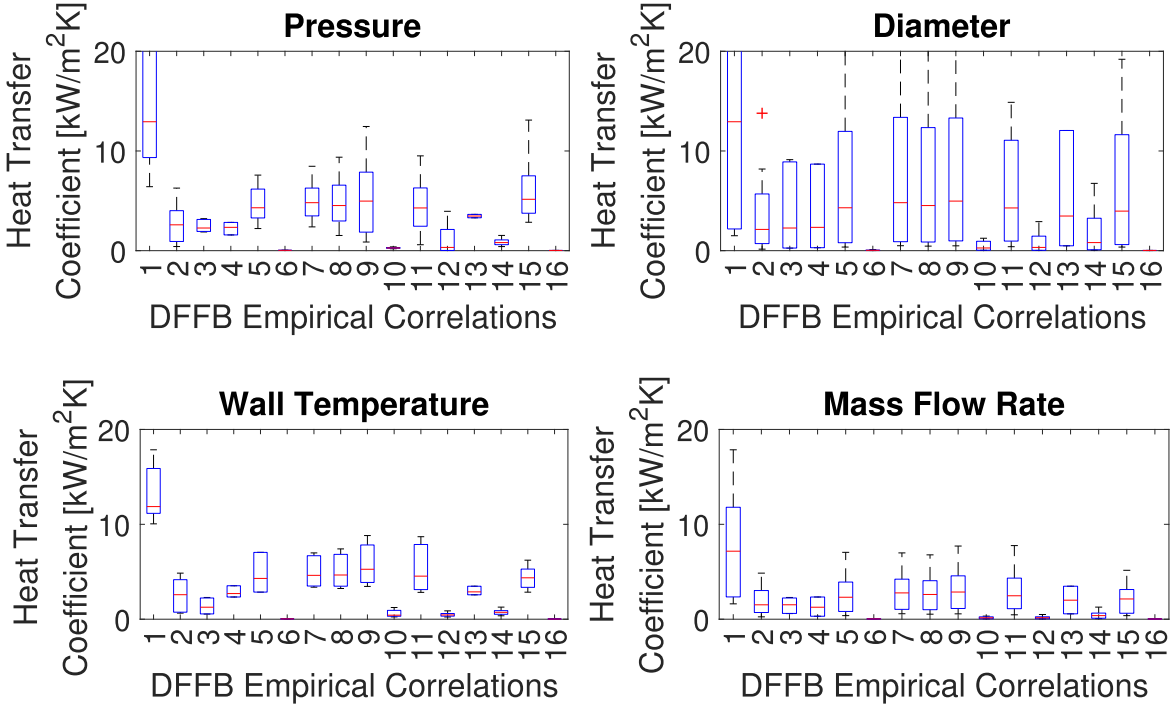

(b)

Fig. 8. Sensitivity analysis results presented as a boxplot for the (a) IAFB and (b) DFFB regime. The numbers of the correlation given in the x-axis correspond to the correlations given Table 9.

Table 10
The effect of a constant heat transfer coefficient on the proposed system.

Heat Transfer Coefficient **[W/m^{2}K]**	Tube Length **[m]**	Evaporator Volume (**x**10^{-6}) **[m^3]**	ORC Volume **[m^3]**	ORC Thermal Efficiency **[%]**
100	7.056	67.90	0.0783	12.71
500	1.752	16.90	0.0781	12.74
1000	1.086	10.40	0.0780	12.75
5000	0.553	5.32	0.0780	12.75
10000	0.486	4.67	0.0780	12.75
50000	0.432	4.16	0.0780	12.75

Table 11
Optimal design parameters for each working fluid.

	p_{max} [bar]	p_{min} [bar]	h_{fin} [mm]	t_{fin} [mm]	f [fins/m]	L_{hot} [mm]	L_{cold} [mm]	N_{hot} [−]	D_{cd} [mm]	N_c [−]	N_{rings} [−]	t_{rec} [mm]	L_{rec} [mm]	t_{ins} [mm]
Toluene	24.65	2.67	0.79	0.72	111	8	100	16	0.21	11	3	22	210	44
MM	11.63	1.856	0.29	0.18	154	26	99	11	0.22	14	3	23	230	62
MDM	7.48	1.031	2.23	0.99	932	5	98	79	0.27	13	3	23	220	62
D4	7.91	1.102	1.71	0.73	863	14	99	8	0.24	18	3	40	140	86
D5	7.02	1.156	5.35	0.97	972	16	100	13	1.48	18	3	24	270	38
D6	5.76	0.997	4.88	0.96	970	18	100	14	1.01	8	5	29	220	36

Table 12
Stowed volume fraction and areal densities of various concentrator types. The areal densities refer only to the primary and secondary concentrators unless otherwise stated and the stowed volume of the optical system is related to the volume of a fixed rigid design type.

Concentrator type	Stowed volume fraction **[%]**	Areal density **[kg/m^2]**	Reference	Comment
Inflatable	1	0.18–1	[25,76,77]	Support structure areal density is unknown for inflatable technologies. Pressurised system mass excluded.
Deployable rigid	25	1.5–3.567	[26,78,79]	Upper bound includes support and tracking mechanisms.
Fixed rigid	100	10–21.2	[31]	Lower bound is a lightweight solution such as carbon-fibre reinforced polymers versus an aluminium design.

heaviest components of the system. Toluene is shown to be the optimal working fluid for reducing the size of the system for a specific energy storage capacity and requires a stowed volume fraction of 18%. This is due to its higher thermal efficiency. However, this advantage is at the expense of faster rotor rotational speeds and smaller rotor blade heights, refer to Table 13. These high speeds, together with the high operating temperature and long lifetime required, eliminate the use of standard ball bearings [80]. Alternative existing high-speed bearings include hydrodynamic, hydrostatic, foil, and magnetic bearings. In the field of micro-gas turbines, foil and hydrostatic (specifically hydroinertia) gas bearings have been identified as possible candidates [81].

Molecular complexity [82] defines the slope of the saturation curve in the T-s plane and is a function of the molecular structure. It increases with number and mass of atoms that form the molecule. All fluids analysed in the optimisation have high molecular complexity and result in dry expansion, which is beneficial in extending the life of the turbine. Fig. 11 illustrates the relationship between molecular complexity and rotor blade height and rotational speed. Fluids with relatively higher molecular complexity require lower enthalpy drops. The size parameter of the turbine is inversely proportional to the enthalpy drop across the turbine and therefore turbine geometry increases with molecular complexity. Rotational speed is proportional to the enthalpy drop and therefore decreases with increasing molecular complexity [6,83]. The thermal efficiency reduces with increasing complexity as the optimal solutions resulted in a decrease in pressure ratio. This is a result of lower critical pressure which reduces the design space, as the upper limit of the maximum cycle pressure is constrained to $0.95p_{cr}$. Fig. 11 also shows the potential inverse relationship between shared power density and molecular complexity. This is due to the decrease in thermal efficiency and thus decrease in electrical power output with increasing fluid molecular complexity. Toluene and linear siloxanes with relatively lower molecular complexity have higher shared power densities which is more advantageous for small satellites, with blade heights larger than the manufacturing limit. Fluids with lower molecular complexities would result in rotor geometries that are not feasible at the power level and operating temperature considered in this study.

A proportional linear relationship can be derived from the optimal solutions system volume and mass with respect to molecular complexity, as shown in Fig. 12. The linear trends have an r-squared fit of 0.90 and 0.81 for the system mass and volume respectively. This proportional relationship is mainly due to the decrease of thermal efficiency, which increases the power input required for the same design constraints. The increase in power input needed means that a larger optical system is required which has the most significant effect of the proposed system. For the application considered in this study, fluids with high molecular complexity are required to meet the manufacturing limit of microturbines. However, out of the working fluids considered in this study, fluids with relatively lower molecular complexity are desired to maximise thermal efficiency and therefore minimise the system mass and volume.

Table 13 illustrates that the system using the Toluene working fluid has a total specific power of 3.6W/kg, which does not compete

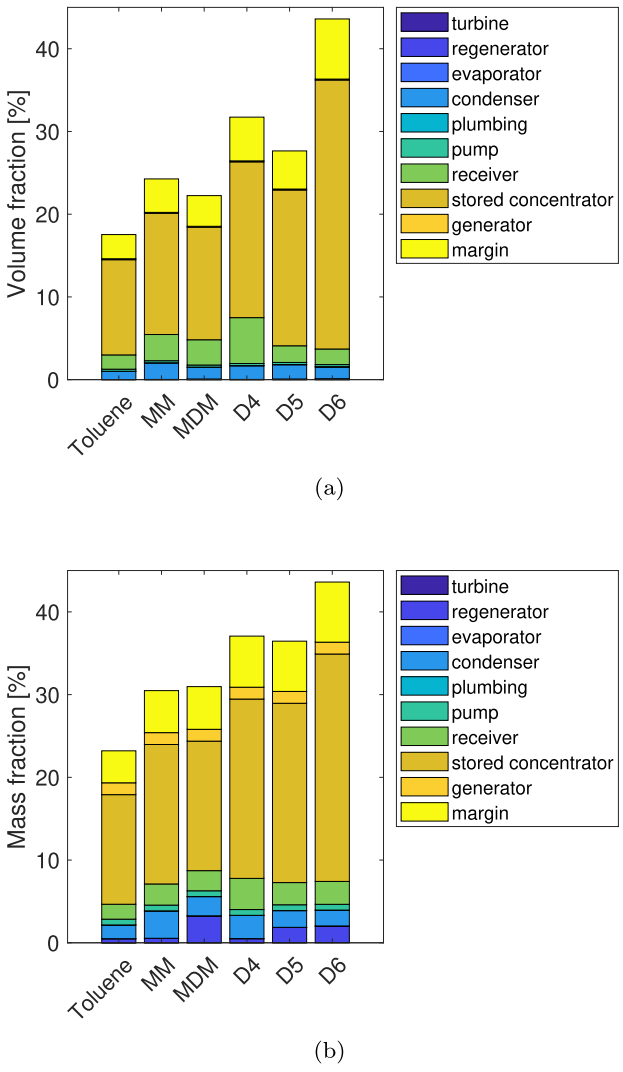

Fig. 9. Optimal solution (a) volume and (b) mass fraction of all the system components relative to the total volume and mass of the satellite.

with solar photovoltaic systems. For example, the SMART-1 mission has an end of life specific density of 24 W/kg (mass includes the solar panels, the Power Control and Distribution Unit and Battery Management Electronics systems). When coupling the micro-ORC system to an STP system the shared specific power is improved to 10.3W/kg assuming that the mass of the concentrator and receiver are part of the propulsion system (shared specific power excludes the receiver and concentrator mass but includes the margin). Despite the low specific power, the advantage to this system comes with the high-temperature thermal energy storage as it provides around 500 Wh/kg of specific energy that could be beneficial in future missions. By using boron instead of silicon, as the PCM, the specific energy could be increased up to 1280 Wh/kg. More efficient and lightweight concentrators, condensers, regenerators, and generators could increase the power density of the system.

Designing micro-turbines is a challenging task due to supersonic flow in the stator, fast rotational speeds and small blade heights. One of the largest unknown parameters is the turbine efficiency of small-scale turbines that utilise organic working fluids. The next section investigates the preliminary total-to-static efficiency of the micro-turbine design using Toluene as a working fluid. Only the Toluene design is evaluated because it is the most suitable working fluid for small satellites due to its low system volume and mass. It also has the smallest turbine size and therefore is the most interesting design to investigate regarding total-to-static efficiency.

5.3. Sensitivity analysis on turbine efficiency

For the micro-turbine design a total-to-static efficiency of 57.38% was found assuming a tip clearance of 75 μm [81] and a surface roughness of 0.05 mm [64]. The fluid was found to operate in the turbulent region with the Reynolds number equal to 1.753×10^5 and 1.346×10^5 for the stator and rotor respectively. This is because the high vapour density and low viscosity of Toluene alleviate the effects of the small blade height. The turbine efficiency used in the optimisation, refer to Table 5, is too high. Therefore, a sensitivity analysis with respect to turbine efficiency is needed to determine the impact of this parameter on the system. Reducing the turbine efficiency, from 65% to 45%, decreases the thermal efficiency of the system by 30.3% and therefore, the electrical power output by 5.16% with respect to reference value (65% turbine

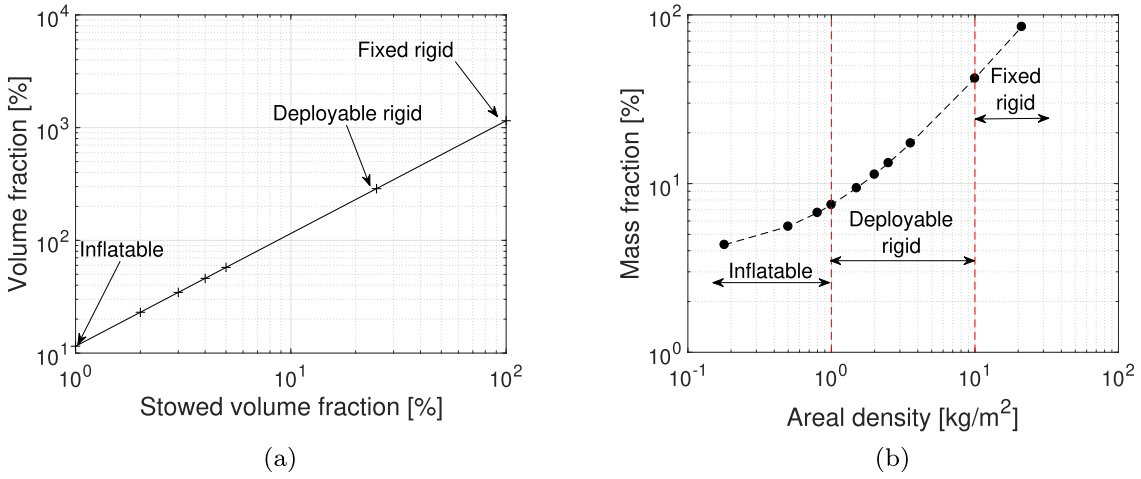

Fig. 10. Optical system (a)volume fraction and (b) mass fraction (including optical fibre bundle) relative to the total volume and mass of the satellite. Table 12 provides the stowed volume fraction and areal density inputs for each concentrator type.

Table 13
Results of the optimal solutions of the optimisation study.

	Rotor blade height [mm]	Rotor rotational speed [krpm]	Thermal efficiency [%]	Total specific power [W/kg]	Shared specific power [W/kg]
Toluene	0.27	772	12.62	3.62	10.29
MM	0.53	306	9.86	2.70	7.45
MDM	0.66	210	9.19	2.56	6.14
D4	0.69	187	8.03	1.93	6.14
D5	0.84	146	7.24	1.87	5.63
D6	0.98	115	6.46	1.56	5.10

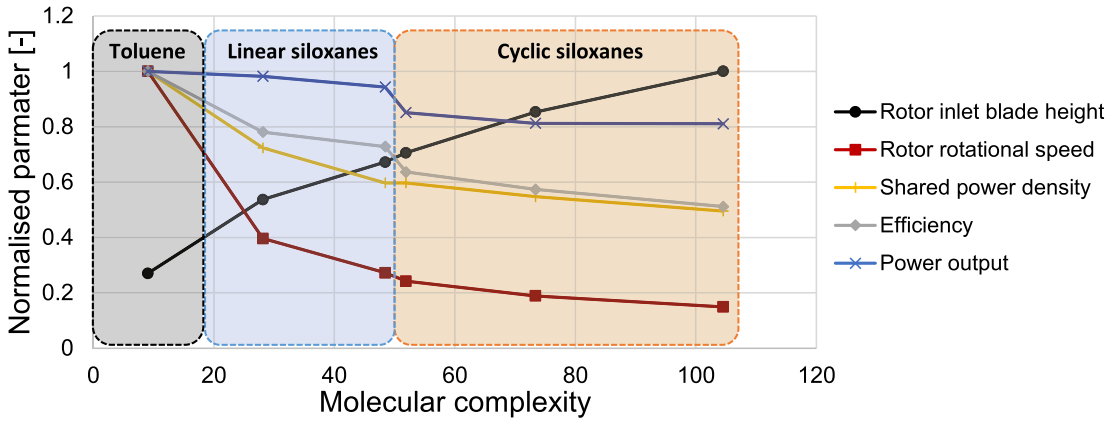

Fig. 11. Normalised output parameters with respect to the maximum values versus molecular complexity, $\sigma = T_{cr}/R(\partial S/\partial T)_{sv,T_r=0.7}$, of the six working fluids optimised in this paper.

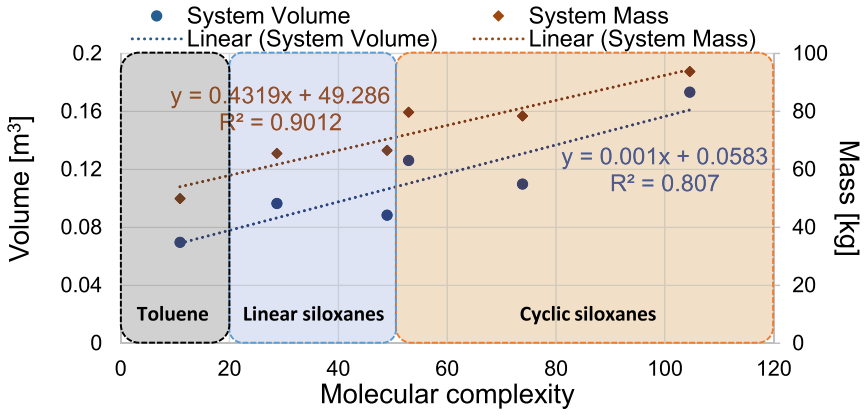

Fig. 12. Linear trends of the proposed system volume and mass with respect to the working fluid molecular complexity, $\sigma = T_{cr}/R(\partial S/\partial T)_{sv,T_r=0.7}$, of the six working fluids optimised in this paper.

efficiency). This, in turn, reduces the shared power density by 18.6%, as shown in Fig. 13. The micro-ORC system mass and volume fraction with respect to satellite mass and volume is 24.6% and 18.4% for the 45% turbine efficiency case and 23.2% and 17.5% for the 65% case. Therefore, these turbine efficiencies are feasible if a system mass and volume fraction of less than 25% and 20% respectively are acceptable, however, this depends on the satellite mission. Additionally, in small-scale turbine designs, heat loss increases with reducing size [81], which would significantly affect the efficiency of the turbine. Heat loss has not been accounted for in this study. However, it is advised that it should be considered in future work along with investigating the possibility of using thermal control from the high-temperature receiver.

6. Conclusions

The study focused on the feasibility of micro-ORC systems for power generation on-board small satellites that use waste energy from a solar thermal propulsion system. An optimisation was performed on six working fluids, accounting for system design, satellite mission, and fluid constraints. From the results, it has been found that Toluene is the optimal fluid in terms of minimising the

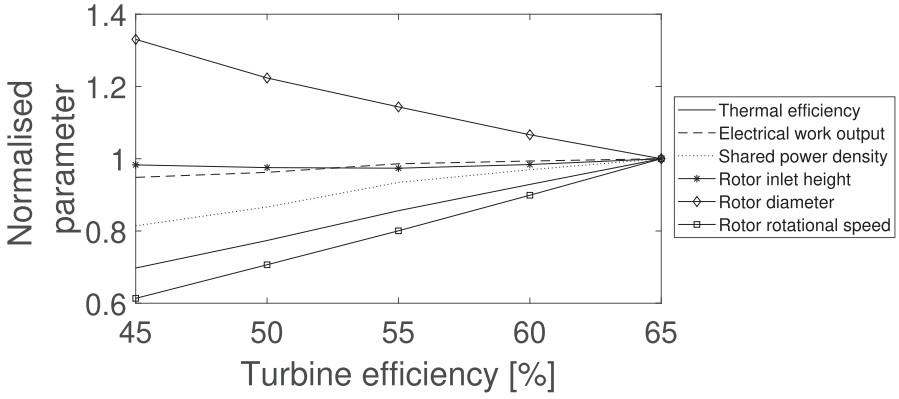

Fig. 13. Normalised turbine output parameters with respect to the 65% case versus turbine efficiency.

volume for a given discharge time. However, the turbine rotor has a small blade height (0.27 mm) and fast rotational speed (772krpm), which makes the attainment of high turbine efficiency challenging. Low turbine efficiencies are expected for micro-turbines mainly due to the large tip clearance of 75 μm, with an total-to-static efficiency of 57.38% obtained for the optimal Toluene solution. The optical system is the largest and heaviest component of the system, promoting the use of inflatable technology. It was found that the critical heat flux is necessary to determine the flow regime inside the evaporator when high-temperature phase change materials are used to better predict the heat transfer and therefore accurately determine the length and volume of the evaporator. However, the heat transfer coefficient of the evaporator has a negligible effect on the complete system volume. Various post CHF empirical equations were evaluated, and the Breen and Westwater and the Bishop correlations were found to provide the closest results to experimental data and mid-range results during the sensitivity analysis. However, the Bromley correlation was adopted instead of the Breen and Westwater because both correlations provide similar heat transfer coefficients under the expected operating conditions but the Bromley reduces the dependency of film boiling heat transfer coefficient on the surface tension.

Recommended future work is to conduct experimental testing and in-depth modelling of the evaporator-receiver coupling to predict the heat transfer better and characterise the off-design and transient effects of the system. Investigation into the performance of micro-turbines is also recommended. The results indicate that micro-ORC systems are feasible on-board small satellites in terms of size and energy storage, and are attractive to missions requiring high specific energies. However, they have low shared specific powers on the order of 10W/kg when coupled to a solar thermal propulsion system. The proposed micro-ORC system would therefore result in a heavier electrical power system for small satellites compared to current state-of-the-art power systems.

CRediT authorship contribution statement

Fiona Leverone: Methodology, Formal analysis, Software, Validation, Visualization, Writing - original draft. **Matteo Pini:** Conceptualization, Validation, Supervision, Writing - review & editing. **Angelo Cervone:** Conceptualization, Supervision, Writing - review & editing. **Eberhard Gill:** Supervision, Writing - review & editing.

Declaration of competing interest

The authors declare that they have no known competing financial interests or personal relationships that could have appeared to influence the work reported in this paper.

Acknowledgement

The authors would like to thank Prof. Manfredo Gherardo Guilizzoni and Dr. Andrea Spinelli for their fruitful discussion on two-phase flow and organic fluids.

References

[1] R. Surampudi, J. Blosiu, P. Stella, J. Elliott, J. Castillo, T. Yi, J. Lyons, M. Piszczor, J. McNatt, C. Taylor, E. Gaddy, S. Liu, E. Plichta, C. Iannello, Solar power technologies for future planetary science missions, Tech. Rep., NASA (2017). JPL D-10136.
[2] R. Surampudi, J. Blosiu, R. Bugga, E. Brandon, M. Smart, J. Elliott, J. Castillo, T. Yi, L. Lee, M. Piszczor, T. Miller, C. Reid, C. Taylor, S. Liu, E. Plichta, C. Iannello, Energy Storage Technologies for Future Planetary Science Missions, Tech. rep, NASA, Pasadena, Califronia, 2017. JPL D-101146.
[3] M.D. Antonio, C. Shi, B. Wu, A. Khaligh, Design and optimization of a solar power conversion system for space applications, IEEE Trans. Ind. Appl. 55 (3) (2019) 2310–2319.
[4] K. Montgomery, J. Buckner, Z. Levin, J. Cromer, D. Wilt, Advanced space power technology development at the air force research laboratory, in: AIAA Scitech 2019 Forum, 2019, p. 1671.
[5] G. Sebestyen, S. Fujikawa, N. Galassi, A. Chuchra, Low Earth Orbit Satellite Design, Springer, 2018.
[6] F. Leverone, A. Cervone, M. Pini, E. Gill, P. Colonna, Feasibility of an integrated solar thermal power and propulsion system for small satellites, in: 68th International Astronautical Congress, Adelaide, 2017.
[7] F. Leverone, A. Cervone, E. Gill, Cost analysis of solar thermal propulsion systems for microsatellite applications, Acta Astronaut. 155 (2019) 90–110.
[8] M. Preißinger, D. Brüggemann, Thermal stability of hexamethyldisiloxane (MM) for high-temperature organic Rankine cycle (ORC), Energies 9 (3) (2016) 183.
[9] P. Colonna, N.R. Nannan, A. Guardone, E.W. Lemmon, Multiparameter equations of state for selected siloxanes, Fluid Phase Equil. 244 (2) (2006) 193–211.
[10] G. Angelino, C. Invernizzi, Cyclic methylsiloxanes as working fluids for space power cycles, J. Sol. Energy Eng. 115 (3) (1993) 130–137.
[11] D.L. Trimm, S. Akashah, A. Bishara, M. Absi-Halabi, Catalysts in Petroleum Refining 1989, Studies in Surface Science and Catalysis, Elsevier Science, 1990.
[12] G. Angelino, C. Invernizzi, E. Macchi, Organic working fluid optimization for space power cycles, in: Modern Research Topics in Aerospace Propulsion, Springer, 1991, pp. 297–326.
[13] D. Schubert, Mems-concept using micro turbines for satellite power supply, in: Solar Power, InTech, Ch, 2012, pp. 195–210.
[14] C. Toro, N. Lior, Analysis and comparison of solar-heat driven stirling, brayton and rankine cycles for space power generation, Energy 120 (2017) 549–564.

[15] N. Muller, L.G. Fréchette, Performance analysis of Brayton and Rankine cycle microsystems for portable power generation, in: ASME 2002 International Mechanical Engineering Congress and Exposition, American Society of Mechanical Engineers, 2002, pp. 513–522.
[16] P. Colonna, E. Casati, C. Trapp, T. Mathijssen, J. Larjola, T. Turunen-Saaresti, A. Uusitalo, Organic Rankine cycle power systems: from the concept to current technology, applications, and an outlook to the future, J. Eng. Gas Turbines Power 137 (10) (2015) 100801.
[17] S. Lecompte, H. Huisseune, M. Van Den Broek, B. Vanslambrouck, M. De Paepe, Review of organic rankine cycle (orc) architectures for waste heat recovery, Renew. Sustain. Energy Rev. 47 (2015) 448–461.
[18] J. Harinck, P. Colonna, A. Guardone, S. Rebay, Influence of thermodynamic models in two-dimensional flow simulations of turboexpanders, J. Turbomach. 132 (1) (2010) 11001.
[19] A. Uusitalo, T. Turunen-Saaresti, A. Guardone, A. Grönman, Design and flow analysis of a supersonic small scale ORC turbine stator with high molecular complexity working fluid, in: ASME Turbo Expo 2014: Turbine Technical Conference and Exposition, American Society of Mechanical Engineers, 2014. V03BT26A004–V03BT26A004.
[20] L.G. Fréchette, C. Lee, S. Arslan, Development of a mems-based rankine cycle steam turbine for power generation: project status, Proc. Power MEMS 4 (2004) 28–30.
[21] S. Roudy, L. Frechette, Energy Scavenging and Nontraditional Power Sources for Wireless Sensor Networks, Wiley, 2005.
[22] M. Orosz, Small scale solar ORC system for distributed power in Lesotho, in: Johannesburg, South Africa: Solar World Congress, 2009.
[23] M. Liamini, H. Shahriar, S. Vengallatore, L.G. Fréchette, Design methodology for a rankine microturbine: thermomechanical analysis and material selection, J. Microelectromechanical Syst. 20 (1) (2010) 339–351.
[24] J. Kreider, Medium and High Temperature Solar Processes, Energy Science and Engineering, Academic Press, Inc., New York, 1979.
[25] P. Henshall, A Proposal to Develop and Test a Fibre-Optic Coupled Solar Thermal Propulsion System for Microsatellites, Tech. Rep. 0704-0188, Surrey University Guildford, United Kingdom, 2006.
[26] M. Gilpin, High Temperature Latent Heat Thermal Energy Storage to Augment Solar Thermal Propulsion for Microsatellites, Ph.D. thesis, University of Southern California, 2015.
[27] P. Olla, Space Technologies for the Benefit of Human Society and Earth, nv - 1 onl Edition, Springer, Dordrecht, 2009.
[28] L.S. Mendoza Castellanos, G.E. Carrillo Caballero, V.R. Melian Cobas, E.E. Silva Lora, A.M. Martinez Reyes, Mathematical modeling of the geometrical sizing and thermal performance of a Dish/Stirling system for power generation, Renew. Energy 107 (2017) 23–35, https://doi.org/10.1016/j.renene.2017.01.020.
[29] T. Nakamura, D. Sullivan, J. McClanahan, J. Shoji, R. Partch, S. Quinn, Solar thermal propulsion for small spacecraft, in: 40th AIAA/ASME/SAE/ASEE Joint Propulsion Conference and Exhibit, July, 2004, pp. 1–11.
[30] T.L. Bergman, F.P. Incropera, D.P. DeWitt, A.S. Lavine, Fundamentals of Heat and Mass Transfer, seventh ed., John Wiley & Sons, 2011.
[31] F. Kennedy, Solar Thermal Propulsion for Microsatellite Manoeuvring, Phd thesis, University of Surrey, 2004.
[32] S. Bahamonde, M. Pini, C. De Servi, A. Rubino, P. Colonna, Method for the preliminary fluid dynamic design of high-temperature mini-organic rankine cycle turbines, J. Eng. Gas Turbines Power 139 (8) (2017) 82606.
[33] P. Colonna, T.P. der Stelt, FluidProp: a Program for the Estimation of Thermo Physical Properties of Fluids, Section, Delft University of Technology, Delft, The Netherlands, 2004. V3.2, http://www.FluidProp.com.
[34] M.A. Taylor, Plate-fin Heat Exchangers: Guide to Their Specification and Use, Heat Transfer and Fluid Flow Services, 1987.
[35] D.R. Mulville, Structural Design and Test Factors of Safety for Spaceflight Hardware, Tech. Rep., Technical Report NASA-STD-5001, NASA, 1996.
[36] D. Southall, R. Le Pierres, S.J. Dewson, Design considerations for compact heat exchangers, in: Proceedings of ICAPP, vol. 8, ICAPP, 2008, pp. 8–12.
[37] D.P. Shah, K. Ramesh, Sekulic, Fundamentals of Heat Exchanger Design, 2003.
[38] S. Kim, I. Mudawar, Universal approach to predicting saturated flow boiling heat transfer in mini/micro-channels – Part I. Dryout incipience quality, Int. J. Heat Mass Tran. 64 (2013) 1226–1238.
[39] S. Kim, I. Mudawar, Universal approach to predicting saturated flow boiling heat transfer in mini/micro-channels – Part II. Two-phase heat transfer coefficient, Int. J. Heat Mass Tran. 64 (2013) 1239–1256.
[40] S. Kim, I. Mudawar, Universal approach to predicting two-phase frictional pressure drop for mini/micro-channel saturated flow boiling, Int. J. Heat Mass Tran. 58 (1–2) (2013) 718–734.
[41] G.F. Hewitt, J.-M. Delhaye, N. Zuber, Multiphase Science and Technology, vol. 2, Springer Science & Business Media, 2013.
[42] B.P. Breen, J.W. Westwater, Effect of diameter of horizontal tubes on film boiling heat transfer, AICHE Symp. Ser. 58 (1962) 67–72.
[43] S. Kim, I. Mudawar, Universal approach to predicting heat transfer coefficient for condensing mini/micro-channel flow, Int. J. Heat Mass Tran. 56 (1–2) (2013) 238–250.
[44] S. Kim, I. Mudawar, Universal approach to predicting two-phase frictional pressure drop for adiabatic and condensing mini/micro-channel flows, Int. J. Heat Mass Tran. 55 (11–12) (2012) 3246–3261.
[45] M.M. Shah, Comprehensive correlation for dispersed flow film boiling heat transfer in mini/macro tubes, Int. J. Refrig. 78 (2017) 32–46.
[46] R.K. Shah, A.L. London, Laminar Flow Forced Convection in Ducts: a Source Book for Compact Heat Exchanger Analytical Data, Academic press, 2014.
[47] S. Kakaç, R. Shah, W. Aung, Handbook of Single-phase Convective Heat Transfer, John Wiley & Sons, New York, 1987.
[48] S.M. Marco, L.S. Han, A note on limiting laminar Nusselt number in ducts with constant temperature gradient by analogy to thin-plate theory, Trans. ASME 77 (1955) 625–630, 1955.
[49] B.S. Petukhov, T.F. Irvine, J.P. Hartnett, Advances in Heat Transfer, vol. 6, Academic, New York, 1970, pp. 503–504, 6.
[50] V. Gnielinski, New equations for heat and mass transfer in the turbulent flow in pipes and channels, NASA STI/Recon Tech. Rep. A 75 (1975) 8–16.
[51] D. Gilmore, Spacecraft Thermal Control Handbook, Volume I: fundamental technologies, American Institute of Aeronautics and Astronautics, Inc., 2002.
[52] Aspen Technology, Exchanger Design and Rating, V8.8, 2015.
[53] S. Grauso, R. Mastrullo, A.W. Mauro, J.R. Thome, G.P. Vanoli, Flow pattern map, heat transfer and pressure drops during evaporation of R-1234ze (E) and R134a in a horizontal, circular smooth tube: experiments and assessment of predictive methods, Int. J. Refrig. 36 (2) (2013) 478–491.
[54] M.K. Bashar, K. Nakamura, K. Kariya, A. Miyara, Experimental study of condensation heat transfer and pressure drop inside a small diameter microfin and smooth tube at low mass flux condition, Appl. Sci. 8 (11) (2018) 2146.
[55] A. Greco, Convective boiling heat transfer of pure and mixed refrigerants within plain horizontal tubes: an experimental study, Adv. Multiphase Flow Heat Transfer 2 (2010) 216.
[56] Y. Yan, H. Lio, T. Lin, Condensation heat transfer and pressure drop of refrigerant R-134a in a plate heat exchanger, Int. J. Heat Mass Tran. 42 (6) (1999) 993–1006.
[57] M.E. Nakla, D.C. Groeneveld, S.C. Cheng, Experimental study of inverted annular film boiling in a vertical tube cooled by R-134a, Int. J. Multiphas. Flow 37 (1) (2011) 67–75.
[58] N.H. Nguyen, S.-K. Moon, An improved heat transfer correlation for developing post-dryout region in vertical tubes, Nucl. Eng. Technol. 47 (4) (2015) 407–415.
[59] K.M. Becker, C.H. Ling, S. Hedberg, G. Strand, An Experimental Investigation of Post Dryout Heat Transfer, Tech. rep., Royal Inst. of Tech., 1983.
[60] D. Simon, Biogeography-based Optimization, 2009. https://academic.csuohio.edu/simond/bbo/, 2018-05-29.
[61] H. Ghaebi, M. Yari, S.G. Gargari, H. Rostamzadeh, Thermodynamic modeling and optimization of a combined biogas steam reforming system and organic Rankine cycle for coproduction of power and hydrogen, Renew. Energy 130 (2019) 87–102.
[62] A. Messac, Optimization in Practice with MATLAB®: for Engineering Students and Professionals, Cambridge University Press, 2015.
[63] A.C. Caputo, P.M. Pelagagge, P. Salini, Joint economic optimization of heat exchanger design and maintenance policy, Appl. Therm. Eng. 31 (8–9) (2011) 1381–1392.
[64] J.F. Suhrmann, D. Peitsch, M. Gugau, T. Heuer, U. Tomm, Validation and development of loss models for small size radial turbines, in: ASME Turbo Expo 2010: Power for Land, Sea, and Air, American Society of Mechanical Engineers Digital Collection, 2010, pp. 1937–1949.
[65] M. Pini, T. Van der Stelt, Special Turbomachinery Design Optimization Laboratory (Stodola), 2019.
[66] C.M. De Servi, M. Burigana, M. Pini, P. Colonna, Design method and performance prediction for radial-inflow turbines of high-temperature mini-Organic Rankine Cycle power systems, J. Eng. Gas Turbines Power 141 (9) (2019), 091021.
[67] C. Rodgers, Mainline Performance Prediction for Radial Inflow Turbines, Von Karman Inst. Lecture Series, 1987.
[68] F. Alshammari, Radial Turbine Expander Design, Modelling and Testing for Automotive Organic Rankine Cycle Waste Heat Recovery, Ph.D. thesis, Brunel University London, 2018.
[69] C.A.M. Ventura, P.A. Jacobs, A.S. Rowlands, P. Petrie-Repar, E. Sauret, Preliminary design and performance estimation of radial inflow turbines: an automated approach, J. Fluid Eng. 134 (3) (2012) 31102.
[70] J.E. Coppage, F. Dallenbach, Study of Supersonic Radial Compressors for Refrigeration and Pressurization Systems, Tech. rep., Garrett Corp. Airesearch Manufacturing Company, 1956.
[71] D.S. Musgrave, The prediction of design and off-design efficiency for centrifugal compressor impellers, in: Performance Prediction of Centrifugal Pumps and Compressors, 1979, pp. 185–189.
[72] H.E. Rohlik, Analytical Determination of Radial Inflow Turbine Design Geometry for Maximum Efficiency, National Aeronautics and Space Administration, 1968.
[73] C.F. Colebrook, T. Blench, H. Chatley, E.H. Essex, J.R. Finniecome, G. Lacey, J. Williamson, G.G. Macdonald, Correspondence. turbulent flow in pipes, with particular reference to the transition region between the smooth and rough pipe laws.(includes plates), J. Inst. Civ. Eng. 12 (8) (1939) 393–422.
[74] A. Whitfield, F. Wallace, Study of incidence loss models in radial and mixed-flow turbomachinery, in: Conference on Heat and Fluid Flow in Steam and Gas Turbine Plant, Coventry, England, 1973, pp. 122–128.
[75] N.C. Baines, A meanline prediction method for radial turbine efficiency, in: IMECHE Conference Transactions, vol. 11, Mechanical Engineering Publications, 1998, pp. 45–56.
[76] J. Pearson Jr., P. Gierow, D. Lester, Near term in-space demonstration of an

inflatable concentrator, in: 37th Aerospace Sciences Meeting and Exhibit, 1999, p. 1073.
[77] H. Sahara, M. Shimizu, Solar thermal propulsion system for microsatellites Orbit transferring, in: 40th AIAA/ASME/SAE/ASEE Joint Propulsion Conference and Exhibit, Joint Propulsion Conferences, American Institute of Aeronautics and Astronautics, 2004.
[78] R.K. Shaltens, L.S. Mason, Early results from solar dynamic space power system testing, J. Propul. Power 12 (5) (1996) 852–858.
[79] P. Frye, C. Kudija, Integrated solar upper stage engine ground demonstration test results and data analysis, in: 34th AIAA/ASME/SAE/ASEE Joint Propulsion Conference and Exhibit, 1998, p. 3958.
[80] O. Dessornes, S. Landais, R. Valle, A. Fourmaux, S. Burguburu, C. Zwyssig, Z. Kozanecki, Advances in the development of a microturbine engine, J. Eng. Gas Turbines Power 136 (7) (2014) 71201.
[81] K. Isomura, M. Murayama, S. Teramoto, K. Hikichi, Y. Endo, S. Togo, S. Tanaka, Experimental verification of the feasibility of a 100 W class micro-scale gas turbine at an impeller diameter of 10 mm, J. Micromech. Microeng. 16 (9) (2006) S254.
[82] C.M. Invernizzi, Closed Power Cycles, vol. 11, Springer, 2013.
[83] C. Hall, S.L. Dixon, Fluid Mechanics and Thermodynamics of Turbomachinery, Butterworth-Heinemann, 2013.